

Jovian Clouds and Haze

Robert A. West, Kevin H. Baines, A. James Friedson

Jet Propulsion Laboratory, California Institute of Technology

Don Banfield

Cornell University

Boris Ragent

NASA Ames Research Center

Fred W. Taylor

Oxford University

5.1 INTRODUCTION

At wavelengths from the near-ultraviolet (0.2 μm) to the infrared (5 μm) Jupiter's appearance is dominated by contrasts produced by clouds and haze. It is important to understand the distribution and optical and physical properties of cloud and haze particles because they play a major role in the radiative heat budget, and they can tell us about atmospheric processes such as stratospheric circulation and tropospheric meteorology. The study of jovian clouds and haze also provides insight needed for interpretation of spectra of extrasolar giant planets. This chapter is concerned with the chemical and physical properties of cloud and haze particles, their vertical and horizontal distributions, their radiative properties, and their microphysical properties. These topics are entwined with the chemistry and composition of the troposphere and stratosphere, atmospheric dynamics and auroral processes that are the principal subjects of Chapters 4, 6, 7 and 9.

This chapter is divided into two main sections focusing on clouds and haze in the troposphere and stratosphere. The term "haze" will be used for a very dispersed and nearly uniform, ubiquitous layer of sub-micron particles in the upper troposphere (200–500 mbar) and for particles in the stratosphere (pressure less than 100 mbar). We use the term "clouds" for the more variable clouds of larger particles at deeper levels. These are further subdivided into the categories of chemical composition, physical properties, distribution, and microphysics. Both observations and theoretical treatments of each of these are given, but with emphasis on the observations since it is in that domain that most of the information resides.

There is a large body of observational evidence relevant to studies of jovian clouds, with contributions from ground-based and earth-orbital telescopes over a long period of time, and major concentrated bursts from the *Pioneer*, *Voyager*, *Galileo* and *Cassini* spacecraft. In this chapter we give emphasis to research activity after 1986. The reader

is encouraged to consult West *et al.* (1986) for a review of theory and observational results from *Pioneer*, *Voyager* and ground-based studies prior to 1986.

5.2 TROPOSPHERIC CLOUDS

5.2.1 Thermochemical Equilibrium Theory and Cloud Microphysical Theory

Our expectations of the types and locations of jovian condensate clouds are rooted in thermochemical equilibrium theory. Lewis (1969) and Weidenschilling and Lewis (1973) were the first to infer cloud compositions and altitudes from detailed models of Jupiter's composition coupled with thermochemical equilibrium arguments. Of particular interest are constituents (N, S, and O) that can combine with H to form water (H_2O), ammonia (NH_3), hydrogen sulfide (H_2S) and ammonium hydrosulfide (NH_4SH). These constituents were thought to be near solar composition or perhaps enhanced relative to hydrogen. Methane is observed by remotely sensed measurements and by the *Galileo* probe to be enhanced over solar by a factor of 3 (Atreya *et al.* 1997; see Chapter 4). Methane does not condense and so should be representative of the bulk mixing ratio. Enhancements of N, S, and O are therefore also expected, but the difficulty has been to interpret observations that are sensitive to the mixing ratios of these constituents in regions where their gas-phase abundance is depleted by condensation.

First we focus briefly on current thermochemical equilibrium models as a starting point for understanding condensate clouds. Figure 5.1 shows idealized cloud structures from Atreya *et al.* (1997) for various assumptions about the mixing ratio of condensable species relative to solar abundance. Under solar or twice-solar mixing ratios for the condensable species, we would expect to find a water–ammonia solution cloud with a base near 6 bar, an ammonium hydrosulfide cloud with a base near 2.2 bar, and an ammonia ice cloud

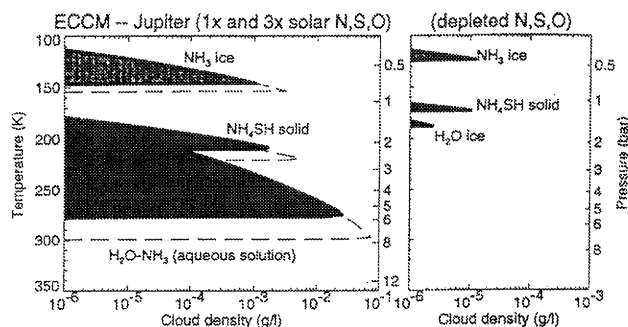


Figure 5.1. Thermochemical equilibrium profiles from Atreya *et al.* 1997. The layers would be based at altitudes corresponding to pressures of about 0.72, 2.21 and 5.69 bars respectively for assumed solar concentrations (solid curves, left panel), but would fall to 0.84, 2.61 and 7.22 bars for three times solar concentrations (dashed curves), or rise to 0.46–0.53, 1.0–1.34 bars (right panel) for concentrations obtained from measurements made by the *Galileo* Probe Mass Spectrometer (GPMS) (Niemann *et al.* 1996, 1998).

with a base near 0.7 bar. For a dryer atmosphere such as that sampled by the *Galileo* probe (right panel of Figure 5.1), cloud bases move higher in the atmosphere and the cloud amounts are smaller.

Atmospheric dynamics and precipitation lead to situations that can be much more complicated than Figure 1 indicates. We know from terrestrial experience that clouds can be absent or can form in multiple layers at altitudes higher than the nominal cloud base. We might therefore expect to see a mixture of water, ammonium hydrosulfide, and ammonia near the top of the troposphere, with varying mixtures of each of these above their equilibrium base altitudes. The less volatile species may act as seed nuclei for the more volatile condensates at higher altitudes, and may never or rarely be observed spectroscopically if coated by the more volatile materials. Because atmospheric motions and precipitation move condensates vertically, cloud density profiles like those shown in Figure 5.1 are almost never realized in the Earth's atmosphere and we should expect the same for Jupiter. We refer the reader to Chapter 4 for a more thorough discussion of the observational constraints on condensable species.

5.2.2 Condensate Cloud Microphysics

Several attempts have been made to understand condensate cloud microphysical processes in Jupiter's atmosphere in order to estimate from theory cloud-base locations, condensate-density vertical profiles, particle sizes, and precipitation rates. Chief among these are publications by Rossow (1978), Carlson *et al.* (1988), Yair *et al.* (1995), Hueso and Sanchez-Lavega (2001) and Ackerman and Marley (2001). The work by Yair *et al.* and by Hueso *et al.* pertain to jovian moist convective regions whereas the other papers are more general. Ackerman and Marley review much of the previous work, comment on the various assumptions and difficulties and propose a simpler parameterized approach to estimate condensate vertical profiles.

Lewis' thermochemical equilibrium model (extended by Weidenschilling and Lewis) calculated vertical condensate density profiles by assuming any vapor in excess of equi-

librium vapor pressure would condense and remain at the altitude where it condensed. In this model there is no precipitation of condensate particles. Nor is there any transport of condensate particles to higher altitudes due to vertical wind or diffusion. This is also the model adopted by Atreya *et al.* (1997) shown in Figure 5.1.

Rossow (1978) tried to estimate timescales for condensation, coalescence, and sedimentation. Carlson *et al.* (1988) also followed this approach and estimated mean particle size (10–30 micron for the ammonia cloud) but did not calculate condensate vertical profiles. Ackerman and Marley (2001) avoided this approach because it depends sensitively on unknown atmospheric conditions such as the degree of supersaturation that is controlled in an updraft by a balance between adiabatic cooling and condensation. Nevertheless the descriptions of condensation processes provided by Rossow (1978), Carlson *et al.* (1988), Yair *et al.* (1995), Hueso *et al.* (2001) provide a conceptual framework specific to the chemically complex regimes in Jupiter's upper troposphere. Perhaps this framework can be improved in the future by a concerted effort to make better use of knowledge about temperature, composition, cloud and haze structure gleaned from observations.

Ackerman and Marley (2001) show how cloud density profiles appear under a simplified, parameterized description of the cloud microphysics. This approach cannot yield detailed or accurate knowledge of cloud density profiles, but is nonetheless appropriate because it illustrates the nature of the problem commensurate with our primitive understanding of humidity profiles, the role of condensation nuclei, and other fundamentally important cloud physics parameters that vary on short time and spatial scales (at least short compared to our ability to measure and model). Figure 5.2 illustrates how several models of cloud density compare. The important parameter is f_{rain} , a dimensionless parameter that is the ratio of mass-weighted sedimentation velocity to the convective velocity. The parameter takes on the value 0 if there is no sedimentation. To make further progress on understanding cloud density profiles and particle size we must turn to the observations.

5.2.3 Tropospheric Cloud and Haze Distribution: Observational Constraints

With the exception of measurements by instruments on the *Galileo* probe, the only information we have on cloud distribution comes from remote imaging and spectroscopy. Vertical probing of cloud structure is possible by measuring reflectivity in regions of the spectrum where gas absorption limits the depth of penetration of photons. Absorption features by methane and hydrogen gas are well suited to this goal because those constituents are well mixed in the atmosphere. Methane absorption bands between 0.6 and 1 μm have been used extensively because they are broad enough to be captured by narrow-band interference filters and imaged with CCD arrays. Jupiter's spectrum from 0.3 and 1 μm is shown in Figure 5.3, along with methane gas absorption strength (from Karkoschka 1998). A similar plot extending to wavelengths beyond 5 μm can be found in Chapter 4.

The bottom panel of Figure 5.3 provides a measure of the pressure level sensed as a function of wavelength. Rayleigh scattering by molecular hydrogen and helium

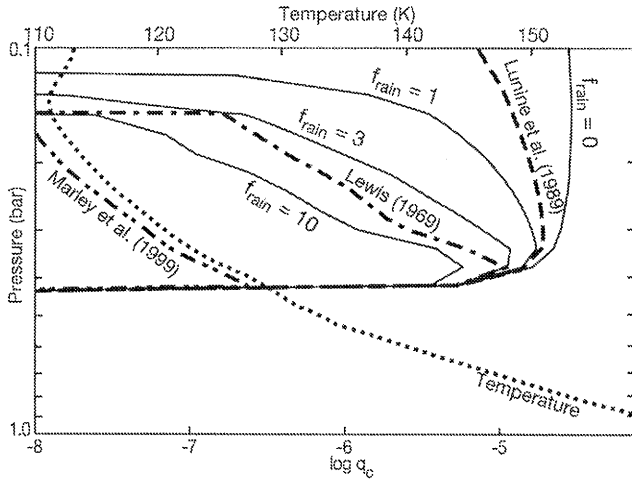


Figure 5.2. Microphysical model profiles of cloud density (mixing ratio by volume) of Jupiter's ammonia cloud from Ackerman and Marley (2001). The parameter q_c is the condensate mixing ratio (moles of condensate per mole of atmosphere). Results are shown for several values of the parameter f_{rain} , which is the ratio of particle sedimentation velocity to convective velocity. Adaptations of models by Marley *et al.* (1999), Lewis (1969) and Lunine *et al.* (1989) are shown.

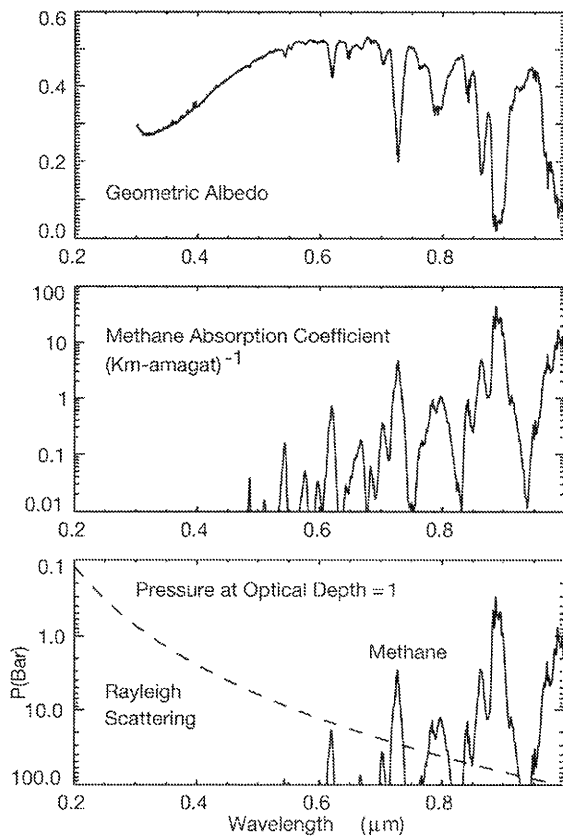


Figure 5.3. Methane gas absorbs sunlight and dominates Jupiter's reflection spectrum at red and near-infrared wavelengths. The top and middle panels were derived from tables provided by Karkoschka (1998).

provides significant opacity in the ultraviolet. For a well-mixed constituent, pressure and optical depth (τ) are related by

$$P = Mg \times 10^{-5} = A_T L_0 \bar{m} g \times 10 / N_a \quad (5.1)$$

and

$$\tau = N\sigma = A_T L_0 f \sigma \times 10^6 \quad (5.2)$$

where P = pressure (bar), M = column mass density (kg m^{-2}) of the gas in the overlying column, g = local gravity (mean value for Jupiter = 24.40 m s^{-2}), A_T = column abundance (m-amagat) of the mixture of H_2 , He and trace gases, L_0 = Loschmidt's number ($2.68719 \times 10^{19} \text{ cm}^{-3}$), \bar{m} = mean molecular weight = $2.27 \times 10^{-3} \text{ kg/mole}$ for an atmosphere with mole fraction 0.86 H_2 and 0.136 He (von Zahn *et al.* 1998), N_a = Avogadro's number ($6.02486 \times 10^{23} \text{ gm mole}^{-1}$), N is the column number density of the gas in the overlying column (molecules m^{-2}), f is the mole fraction of the constituent of interest, and σ = extinction cross section (m^2). Ford and Browne (1973) provided expressions for Rayleigh optical cross sections for H_2 and Chan and Dalgarno (1965) give information for helium. Neglecting the variation of g with latitude, the derived Rayleigh optical depth for this $\text{H}_2 + \text{He}$ mixture is

$$\tau_R/P = 0.0083(1 + 0.014\lambda^{-2} + 0.00027\lambda^{-4})\lambda^{-4} \quad (5.3)$$

for λ in μm and P in bar. This expression can be scaled to any latitude by multiplying by $24.40/g$.

The column abundance of $\text{H}_2 + \text{He}$ is 41 km-amagat at 1 bar. The mixing ratio (mole fraction) of methane is 0.0018 (see Chapter 4) and its column abundance above the 1-bar level is 74 m-amagat.

Some remarks on the limitations of cloud sounding techniques are in order. The use of methane or hydrogen opacity to infer vertical locations of clouds relies on accurate knowledge of the opacities of these constituents as a function of wavelength, temperature and pressure. The observations of Jupiter are mostly from images or spectra that do not resolve the methane line structure, and at visible and near-IR wavelengths the lines are blended, producing a pseudo-continuum absorption that has only weak pressure dependence at wavelengths shorter than $1 \mu\text{m}$. Measurements of the methane absorption coefficient and its temperature dependence are difficult to obtain below $1 \mu\text{m}$ because the absorptions are so weak.

Low spectral resolution laboratory measurements between 0.45 and $1.05 \mu\text{m}$ of room-temperature methane absorption (Fink *et al.* 1977, Giver 1978) show only very weak pressure dependence, and only at wavelengths approaching $1 \mu\text{m}$. The first broadband low-temperature measurements of methane gas were published by Smith *et al.* (1990), who measured the $0.619\text{-}\mu\text{m}$ absorption feature and its adjacent continuum at five temperatures from 100 to 290 K. Singh and O'Brien (1995, 1996) and O'Brien and Cao (2002) have published low-temperature absorption coefficients obtained in the laboratory at 77 K for the $0.727 \mu\text{m}$ and $0.889 \mu\text{m}$ bands. From 0.3 to $1.0 \mu\text{m}$ we can make use of methane coefficients inferred from observations of the giant planets (Karkoschka 1998). The advantage of this technique is that it uses methane coefficients formed by molecular states at the temperatures of the outer planet atmospheres. The dis-

advantage is that the effects of scattering from aerosols must be understood, and this is problematic.

In the near-infrared beyond 0.9 μm , broadband absorption coefficients are functions of both temperature and pressure (or gas density). To efficiently and accurately handle this situation for use in the analysis of vertically-inhomogeneous, scattering atmospheres, the correlated- k technique has been developed (cf. Goody and Yung 1989, Goody *et al.* 1989). Over the past decade, the requisite absorption coefficients for methane have been derived from band-model fits to low-temperature laboratory spectra obtained over a variety of gas pressures (Baines *et al.* 1993, Irwin *et al.* 1996). Coefficients pertaining to temperatures as low as 112 K now exist for much of the near IR (Baines *et al.* 1993). Similar correlated- k coefficients have been derived for gaseous ammonia by Irwin *et al.* (1998a). Correlated- k techniques have been used extensively to interpret *Galileo*/NIMS spectra (e.g., Irwin *et al.* 1998b).

Collision-induced absorption by molecular hydrogen produces distinct broadband spectral features, particularly in the visible near 0.826 μm (Baines and Bergstralh 1986) and the near-infrared near 2.1 μm (Irwin *et al.* 1998b). The spectral behavior of these features are accurately known from theory supported by laboratory measurements, as a function of both pressure and temperature (McKellar and Welsh 1971, Birnbaum and Cohen 1976, Borysow *et al.* 1988, Borysow 1991, 1992, Zheng and Borysow 1995).

The limitations of the technique itself need to be appreciated. The *Galileo* probe Nephelometer can provide precise determination of the altitudes of particles by virtue of in situ measurement. The use of methane or hydrogen absorption from images or spectra of Jupiter can provide only approximate information. The use of many absorption bands whose strengths differ by only a small amount provides the best discrimination for vertical structure. Banfield *et al.* (1998a) make use of an inversion technique based on this approach. With this approach a theoretical delta function cloud sheet (in the vertical dimension) would appear as a gaussian cloud of 1 scale height thickness, but its peak would be located at the pressure of the true cloud to within a small fraction of a scale height.

A sense of the information content provided by methane images can be gleaned from Figure 5.4, which shows Jupiter at three wavelengths that probe progressively deeper into the atmosphere. The effective pressure levels (vertical optical depth = 1 in the absence of cloud opacity) probed by these images are 10, 4, and 0.6 bar, respectively from left to right.

Most evident in Figure 5.4 are Jupiter's bright southern polar hood and equatorial band. The polar hood is bright because of a stratospheric aerosol layer near the 3-mbar pressure level concentrated at high latitude. The north pole also has a hood, but one that appears more diffuse and spread over a larger area than that in the south. In the equatorial region an elevated tropospheric haze (pressure near 200 mbar) is responsible for the brightness. The bright equatorial band is not symmetric about the equator. Jupiter's Great Red Spot on the right edge of each panel is also a region of elevated tropospheric haze.

In the deepest-probing methane band (left panel) the region labeled HS in Figure 5.4 is dark because the column of aerosol above the 6-bar level is less than in the surrounding

area. This is a region very much like that which the *Galileo* probe entered. The middle and right panels show that the upper tropospheric haze covers this region, and the three taken together indicate that the deep clouds are missing. By contrast, the spot labeled W shows the expected characteristics of a water cloud near the 6-bar region. It is bright in the deepest-probing methane band but not seen in the two stronger bands. Yet a third kind of behavior is seen at the location DO (for Dark Oval) which is dark in the two strongest methane bands but not seen in the weakest band, indicating a hole in the middle cloud or top (ammonia) cloud region.

At wavelengths between 1 and 4 μm , methane absorption coefficients vary by many orders of magnitude, providing a basis for cloud sounding over a large pressure range from several bars to about 1 mbar. Opacities provided by molecular hydrogen and ammonia in this spectral range are also important. At longer wavelengths, upwelling thermal radiation can give clues to cloud optical thickness. Spectral regions near 45 μm , 8.5 μm and the 5- μm window region sample successively deeper, from the base of the ammonia cloud near 0.8 bars to the water cloud region near 5 bar. Gierasch *et al.* (1986) inferred cloud properties from *Voyager* IRIS spectra at 5 and 45 μm and found two cloud components. One is variable and is seen at both wavelengths, pointing to a population of 3- to 10- μm radius particles near the ammonia condensation level and serving to modulate 5- μm emission. The other component is distributed uniformly and seen only in the 5- μm data. This is probably caused by a nearly uniform, high tropospheric (200–500 mb) haze of sub-micron particles. Global images from the *Galileo* NIMS experiment in Figure 5.5 show Jupiter's appearance at five wavelengths between 1.61 μm (a continuum region for reflected sunlight) to 4.99 μm (deep thermal emission).

Direct inversion is only possible for the stratosphere of Jupiter where multiple scattering is relatively unimportant. In the troposphere, multiple scattering provides a source function for photons that is no longer coupled in a strictly linear way to the aerosol density. In this regime it is possible to find multiple solutions to the radiative transfer equation that fit the data to within the uncertainties. It is important to understand that a purely objective technique such as direct retrieval is not possible for tropospheric clouds, and the models rely also to some extent on *a priori* assumptions about cloud structure. Some of this non-uniqueness and the various choices of *a priori* assumptions are at the root of current controversies surrounding the cloud structure, to be discussed in more detail below. The difficulty in retrieving cloud information from remote measurements increases with depth in the atmosphere because of obscuration from overlying clouds. Another ambiguity for spectral continuum regions or weak methane bands is the relative importance of absorption by chromophore particles. Inferences about the water cloud from remote measurements are most uncertain.

The review by West *et al.* (1986) provides a starting point for our discussion of observational constraints on tropospheric cloud and haze structure and composition. At the time of that review we had a considerable body of observations from the ground and from the *Pioneer* and *Voyager* spacecraft. There were two views of jovian cloud structure. One view was motivated principally by the appearance of Jupiter at 5 μm (Owen and Terrile 1981), and held that Jupiter's clouds acted much like blackbody emitters at the

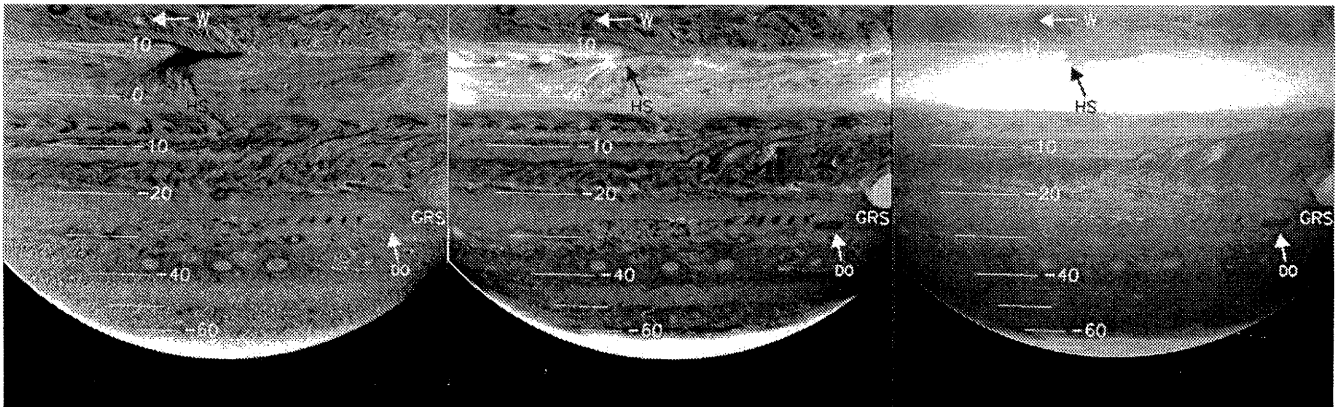


Figure 5.4. The three panels are images of Jupiter in progressively stronger methane bands obtained on December 16, 2000 by the *Cassini* Imaging Subsystem (ISS) Narrow Angle camera. The panel on the left is a contrast-enhanced ratio image using the 0.619- μm methane filter divided by the 0.619- μm continuum filter. The continuum filter has a double-lobe transmission function which passes light in the continuum region from both sides of the 0.619- μm methane band. This design nulls any continuum spectral gradient that might otherwise influence the ratio. The center panel is a ratio of the 0.727- μm methane filter divided by the 0.750- μm continuum filter. The ratio images effectively null any influences due to broadband particle absorption, isolating the influences of cloud height and optical depth. The third image is a single 0.890- μm methane filter image (the effects of methane absorption dominate in that band and so a ratio to the continuum is not helpful). Planetocentric latitudes in 10-degree intervals are indicated, and special features (see text) are labeled.

temperature where they reside. In that model jovian hot spots with effective temperature near 255 K were believed to sample a part of the atmosphere that was essentially cloud-free down to an optically-thick water cloud. Regions with low 5- μm brightness temperature sensed a thick ammonia cloud layer, and regions with intermediate effective temperatures sensed the ammonium hydrosulfide cloud. This picture was augmented by a correlation between 5- μm brightness with visible albedo and color. Regions with 5- μm brightness temperature between about 210 and 240 K (“warm” regions) are generally darker and redder than cool regions. The 5- μm hot spots with brightness temperature 240–260 K are blue-gray in color. This color–brightness–temperature correlation was further reinforced (Owen and Terrile 1981) by the belief that darker colored regions appear to be deeper than whiter, brighter clouds based on visual appearance, analogous to our terrestrial experience.

An opposing view developed from ground-based methane band imagery and from photometry from the *Pioneer* spacecraft. Limb darkening at blue wavelengths is not consistent with a dark colored material confined to the depth of the ammonium hydrosulfide cloud. It requires a chromophore mixed with the ammonia cloud and a deeper cloud in Jupiter’s belts (see Figure 25 of Smith and Tomasko 1984). Methane-band images indicated substantial cloud opacity in the high troposphere (ammonia-cloud region) in belts as well as zones (West and Tomasko 1980).

West *et al.* (1986) tried to resolve this controversy and reconcile visible and infrared imagery by proposing a model with two to eight optical depths (at visible and infrared wavelengths) of small-particle haze covering the high troposphere (in the pressure range 200–500 mb) over all latitudes and variable clouds in the convective part of the troposphere from the base of the ammonia cloud down to the water cloud. This is shown schematically in Figure 5.6. Variability of the deeper clouds accounts for the large variations in cloud opacity seen at 5 μm . The 5- μm hot spots have some cloud opacity in the high troposphere but no water cloud.

The ubiquitous high-altitude aerosol is composed of small (sub-micron or micron) particles which are mostly transparent to 5- μm radiation while particles in the deeper variable clouds are probably larger, up to 100 μm . The haze of small particles is produced in upwelling zones and transported by advection to downwelling belts near the top of the troposphere. Small particles have long lifetimes at this level.

Subsequent studies from the ground and from instruments on the *Galileo* probe and orbiter have largely confirmed the cloud structures proposed in Figure 5.6, but many new details have been added, the first in situ measurements were made, and there are new points of discussion concerning the clouds in the region 0.5 to 2.4 bars and their role in modulating contrasts from the visible to the infrared. In the next sections we summarize findings by instruments on the *Galileo* probe, and orbiter, and from the ground and the Hubble Space Telescope. We wish to focus on some of the new ideas about tropospheric cloud structure and their ties to the data and to the modeling procedure.

5.2.4 Results from the *Galileo* Probe Experiments

The first in situ measurements of the atmosphere and clouds of Jupiter were made from the *Galileo* mission probe. The probe entered the jovian atmosphere on December 7, 1995, at an entry site of about 6.5° N latitude, 4.9° W System III longitude (Young 1998; see also the Erratum, Young 2000). It entered inside and 900 \pm 300 km north of the southern boundary of a 5- μm hot spot (Orton *et al.* 1998). As it descended, instruments aboard the probe made measurements of composition, cloud properties, thermal structure, winds, radiative energy balance, and electrical properties of the jovian atmosphere.

The results of the most direct measurements on the clouds present near the *Galileo* probe during its descent, made by the *Galileo* Nephelometer (NEP) and Net Flux Radiometer (NFR) instruments, have been summarized by Ragent *et al.* (1998) and Sromovsky *et al.* (1998). Plots of

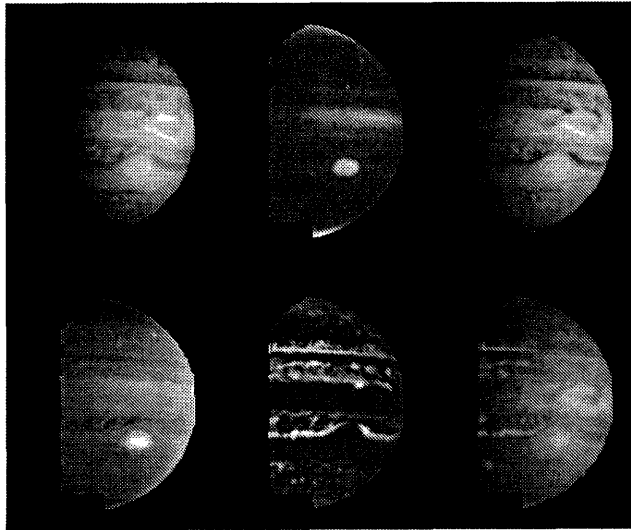


Figure 5.5. These images of Jupiter at various near-infrared wavelengths were taken by the Near-Infrared Mapping Spectrometer (NIMS) during the second orbit (G2) of the *Galileo* spacecraft on September 5, 1996. The differences are due primarily to variations in the altitudes and opacities of the cloud systems. The top left and right images, taken at 1.61 μm and 2.73 μm respectively, are in spectral regions of low molecular absorption giving relatively clear views of the deep atmosphere, down to approximately the 3 bar level. The top center image, at 2.17 μm , shows only the highest altitude clouds and hazes, due to strong absorption by hydrogen. The Great Red Spot, the highest equatorial clouds, a small feature at mid-northern latitudes, and thin, high photochemical polar hazes can be seen. In the lower left image, at 3.01 μm , deeper clouds can be seen but extreme depths are obscured by gaseous ammonia and methane absorption. In the lower middle image, at 4.99 μm , the planet is seen in thermal emission from the deep, warm atmosphere. The false color image (lower right) is a composite in which red areas denote high temperature emission from the deep atmosphere in areas of minimal cloud cover; green denotes cool tropospheric clouds; blue denotes the cold upper troposphere and lower stratosphere. The purplish, yellowish and light blue regions are those with high concentrations of small-particle hazes with various scattering and absorption properties, including high-level hazes of photochemical origin. At the time of going to press a colour version of this figure was available for download from <http://www.cambridge.org/9780521035453>.

signals recorded by the NEP and several NFR channels as a function of ambient pressure are shown in Figure 5.7.

Although the Nephelometer recorded hardly any indications of particles extending from about 0.46 bars to more than 12 bars, it also encountered several distinctive, if very tenuous, cloud-like structures. The NEP instrument was effectively activated at an ambient pressure level at about 0.46 bars (altitude ~ 17.3 km above the altitude at which the ambient pressure is 1 bar) in a decaying, tenuously cloudy structure that declined to a minimum signal at about 0.53 bar, followed by several small peaks down to about 0.59 bars (~ 12.4 km). Table 5.1 provides a summary of the quantitative NEP results for particle radius and other cloud parameters.

After passing through a pressure region extending from 0.60 to 0.75 bars of very small signals that occurred simultaneously in most of the instrument's channels, an increasing particle buildup was encountered made up of several overlapping, distinctive, layered structures extending down to

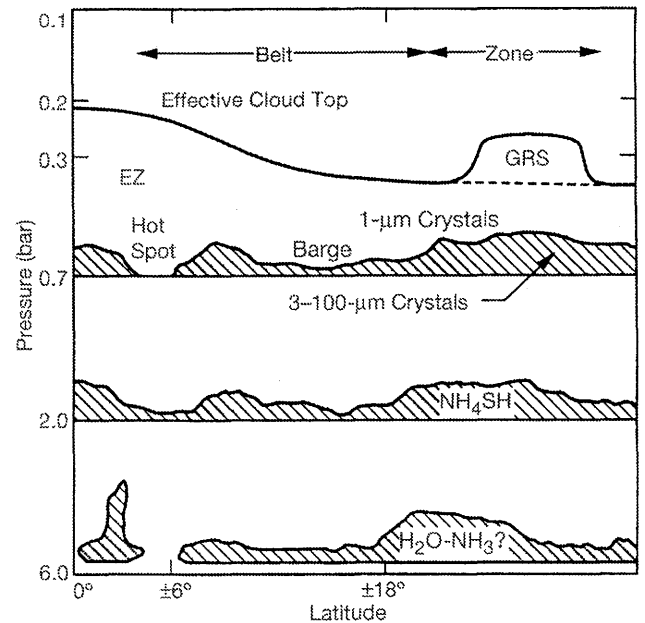


Figure 5.6. This schematic representation synthesizes ideas about tropospheric cloud structure from a large collection of observations after the *Voyager* encounters but before *Galileo* (from West *et al.* 1986). The main features include a ubiquitous upper tropospheric haze of small particles which are probably ammonia but may also have a hydrazine component and clouds of larger particles near the base of the ammonia cloud and in the ammonium hydrosulfide cloud region. These deeper clouds of larger particles vary on short time and space scales and modulate the 5- μm radiance. The water cloud is absent in hot spot regions but may be present in other regions.

a well-defined base at a pressure of 1.34 bars. This structure, although still sparsely populated, produced the largest signals recorded by the Nephelometer during its descent in the jovian atmosphere. Estimated particle properties derived from measurements are listed in Table 5.1.

Between 1.37 and 1.72 bars several very tenuous and vertically thin layers of particles were encountered at pressure levels of 1.40 and 1.52 bars and a denser sharp layer was evident at a pressure of 1.65 bars. No unambiguous values of the particle properties, optical depths, particle number loadings or particle mass loadings were derived for these layers.

Very feeble structure extended from perhaps 2.4 bars down to 3.6 bars or possibly to a somewhat higher pressure (lower altitude). Regent *et al.* (1998) proposed particle radius in the range of 1.0 to 4.0 μm , and optical depths at $\lambda = 0.904$ μm of $\tau \sim 0.09$ –0.13 for this layer (see Table 5.1).

Measurements made by the *Galileo* probe NFR during probe descent also indicated the presence of clouds (Sromovsky *et al.* 1998, Sromovsky and Fry 2002). The probe NFR solar channel signals provided evidence for a cloud above 0.45–0.50 bars composed of particles with an effective radius equal to or less than $r \sim 0.5$ –0.75 μm , and of total optical depth about $\tau \sim 1.5$ –2 at a wavelength of $\lambda \sim 0.5$ μm . In addition, there was a small flux signature in the NFR Channel C (~ 3.5 –5.0 μm wavelength window) consistent with a cloud containing conservatively scattering particles with effective radius of about 3 μm , an optical depth $\tau \sim 1$ at a wavelength of $\lambda \sim 5$ μm , and based at a pressure of

Table 5.1. Altitudes are relative to the 1-bar pressure level. Optical depth (τ) applies to the Nephelometer wavelength 0.904 μm . Values in this table are based on Ragent *et al.* (1998) cases A1–A2 (for the pressure range 0.46–0.53 bar) and B1–B2 (for the range 0.75–1.34 bar) and C1–C2 and C3–C4 (for the range 2.4–3.6 bar).

Particle Mean Radius and Density from *Galileo* Probe Nephelometer Measurements

Altitude (km)	Pressure (bar)	\bar{r} (μm)	τ	Number Density (m^{-3})	Mass Density (kg m^{-3})
12.4 to 17.3	0.46–0.53	0.5–0.9	~ 0.06	$(3.8\text{--}7.5) \times 10^6$	$(1.5\text{--}1.6) \times 10^{-8}$
+7.0 to –7.8	0.75–1.34	0.8–1.1	~ 1.7	$(3.3\text{--}3.4) \times 10^7$	$(2.5\text{--}3.1) \times 10^{-7}$
–26.2 to –39.8	2.4–3.6	1.0–4.0	0.09–0.13	$(1.4\text{--}7.0) \times 10^5$	$(1.2\text{--}3.5) \times 10^{-8}$

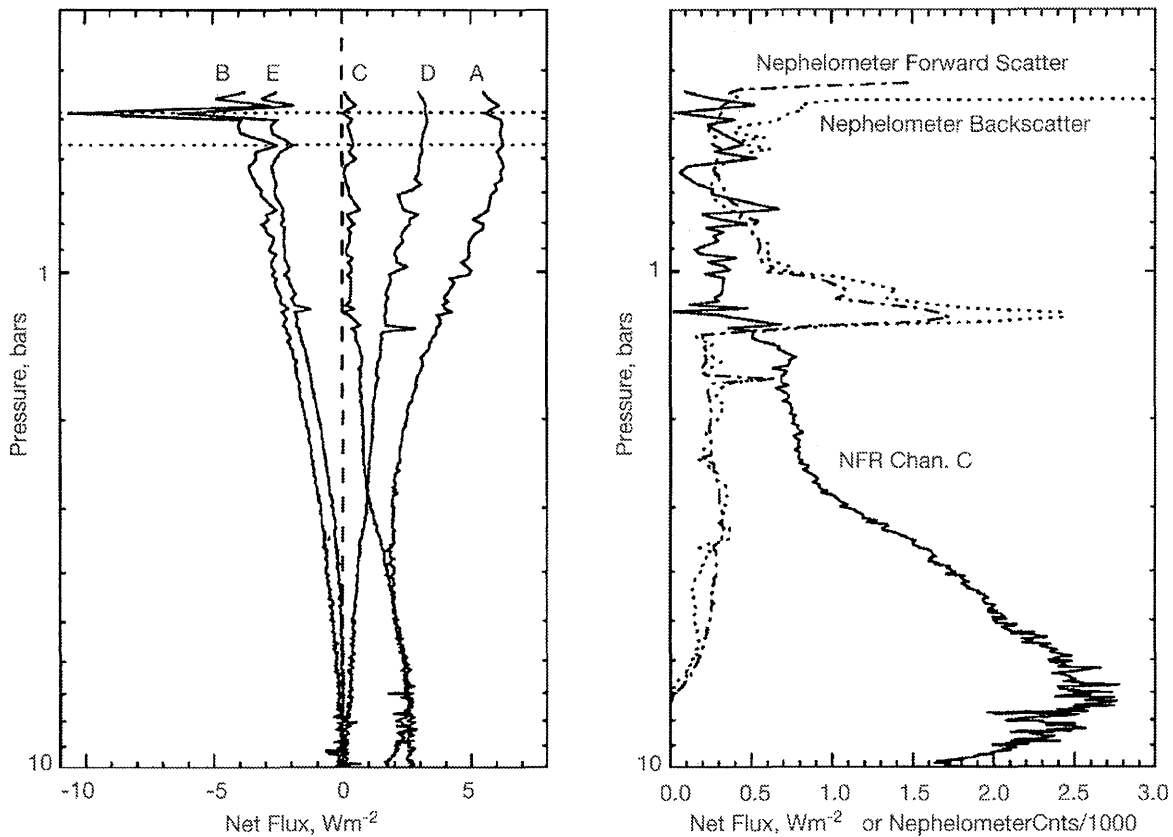


Figure 5.7. *Galileo* probe Net Flux Radiometer (NFR) and Nephelometer profiles during probe descent in a Jupiter atmosphere hot spot. NFR channels B and E spectral response windows were approximately from 0.3–5 μm and 0.6–5 μm , respectively, covering the solar spectral range. Channels A, C and D spectral response windows were from 3–200 μm , 3.5–5 μm and 14–150 μm , respectively, covering the expected thermal range. (Figure 1 of Sromovsky and Fry 2002.) The properties of the upper cloud were inferred from the magnitudes and spectral ratios of the measured solar flux channels seen near 0.5 bars. An optically thick cloud would have made the direct solar beam invisible and prevented such modulations. The presence of a cloud near 1.3 bars, clearly shown by the Nephelometer observations, is also indicated in these data by the gradient in the NFR Channel C profile, indicating radiative heating at the base of the cloud.

1.3–1.4 bars. The NFR found no signatures of a “water” cloud during descent down to beyond the 10-bar range.

In summary, although the *Galileo* probe Nephelometer and Net Flux Radiometer noted the presence of extremely tiny aggregations of particles throughout the probe descent from about 0.46 to beyond 12 bars, the major discoveries included a tenuous cloud based at about 0.5 bar, a small well-defined cloud, sharply based at 1.34 bars, several thin clouds of small vertical extent, especially one at 1.6 bar, and a very tenuous structure of particles in the region of about 2.4 to 3.6 bars. No compelling evidence for a deep

water cloud was found by either the NEP or the NFR. All of the NEP signals received were very small, even in the densest clouds detected, signals that would correspond on Earth to typical “visibilities” of the order of a few to 100 km. The results of these two in situ experiments, with the exception of minor details and altitude locations, indicate very good semi-quantitative agreement with the empirical picture presented by West *et al.* (1986), discussed above for a 5- μm hot spot.

The most immediately plausible explanation for the depletions of condensables and the appearance of the clouds

encountered by the probe in the hot spot was that strong atmospheric dynamics, i.e., atmospheric motions, were present. Original suggestions all involved the presence of a severe downdraft from an overlying, surrounding, dry atmosphere into the hot spot (West *et al.* 1986). The dry overlying atmosphere is formed, presumably, by upwelling air outside of the hot spot that has lost its volatile condensables due to condensation during its rising motion, and driven, perhaps, by moist convective processes (Niemann *et al.* 1996, Showman and Ingersoll 1998, Atreya *et al.* 1999, Gierasch *et al.* 2000, Ingersoll *et al.* 2000, Hueso and Sanchez-Lavega 2001). These suggestions, criticisms and other models are discussed in more detail in Chapter 6. A further implication is that cloud altitudes and densities derived for hot spots are unlikely to be reproduced in regions outside of hot spots.

5.2.5 Galileo NIMS Observations and Results

The Near-Infrared Mapping Spectrometer or NIMS (Carlson *et al.* 1992) on *Galileo* imaged Jupiter at up to 408 wavelengths from 0.7 to 5.2 μm . Across this range, which is rich in methane, hydrogen, and gaseous and solid ammonia absorptions among others, the appearance of the planet varies markedly, as shown by the examples at five wavelengths in Figure 5.5. The spectra extend from the region dominated by reflected sunlight into the 5- μm “window” where thermal emission dominates, and sound vertically from near the water cloud up to the haze that lies near the tropopause.

The high tropospheric haze, with its top near 200 mbar, is thickest in a wide band over the boundary between the Equatorial Zone and the North Equatorial Belt, from about 0° to 9° N (Figures 5.4 and 5.5, upper right panel). The fact that it is not centered on the equator was also noted by Banfield *et al.* (1998a) who remarked that the same offset is found for the hydrogen ortho-para fraction, both pointing to relatively strong upwelling near the tropopause in this latitude band.

This haze, and the ammonia cloud which lies below and possibly contiguous with it, are semitransparent at thermal infrared wavelengths. The most direct evidence for this is the color temperature of the emission from the cloudy zones, which is inconsistent with a source as cool as the ammonia cloud (Drossart *et al.* 1998). Day-night differences show that reflected solar radiation contributes to the 5- μm intensity in the belts on the dayside, but the NIMS 5- μm spectra are biased more towards the blue end of the spectrum than is the Planck function for the expected temperature of the ammonia cloud, even on the nightside of the planet. Most of the radiance being measured by the spectrometer must therefore have originated below the ammonia cloud, and must propagate through it.

Model fits to NIMS nightside spectra by Drossart *et al.* produced a typical value of 0.002 for the transmission and 0.15 for the reflectivity of the ammonia cloud in the belts at wavelengths near 5 μm . They also set an upper limit of 0.79 bars for the pressure at the top of this cloud. Histograms of the brightness of Jupiter at 5 μm on the nightside (Cameron-Smith 1998) show peaks centered on 165 K and 240 K, corresponding to the zones and belts respectively. The narrowness of the cooler peak, in contrast to the much broader warm peak, suggests that the properties of the zone clouds are remarkably uniform over a wide area on Jupiter.

Formal retrievals of the vertical run of cloud opacity which fit the NIMS 5- μm spectra (Irwin *et al.* 1998b, 2001) find the main cloud opacity at about the level the thermochemical models predict for ammonium hydrosulfide, i.e., around 1.5 bars, which is below the optically thinner ammonia clouds. The latter extend upwards from about 0.72 bars and merge into the haze near the tropopause, at about 0.26 bars. The spectral behavior of the NH_4SH cloud is consistent with large particles, and it is also the main variable opacity source responsible for the belt-zone structure at thermal infrared wavelengths. This major result was confirmed by Irwin and Dyudina (2002), who analyzed NIMS spectra using empirical orthogonal functions and found that only three are needed to describe the variations from place to place. The three EOFs correspond to variations in the ammonium hydrosulfide cloud opacity, the upper tropospheric haze opacity, and the ammonia abundance. The first of these factors accounts for most of the observed variations in 5- μm brightness. The effect of the haze opacity is much less, and in this analysis is found to be anticorrelated with the main cloud opacity, i.e., the haze is thicker over the belts, those regions which are dark at visible wavelengths. We describe in the section on particle composition an additional spectral signature in the NIMS data that reveals the presence of ammonia ice.

The water cloud predicted by the thermochemical models would, on the temperature profile measured by the *Galileo* probe, lie at a pressure of around 5 bars. This is below the maximum depth sounded by NIMS, except possibly in hot spots, where the water cloud is likely to be reduced, depressed, or eliminated altogether by strong downwelling. It is not surprising, therefore, that NIMS has made no firm detection of deep water clouds.

5.2.6 Galileo SSI Observations and Results

Galileo's Solid State Imager (SSI) contributed to cloud structure studies with a combination of high spatial resolution and multi-angle viewing in filters sampling two methane bands (at 0.889 and 0.727 μm) and in the continuum at 0.756 μm and 0.410 μm . The two methane filters and 0.756- μm continuum filter are similar to those used in the right and middle panels of Figure 5.4. The weighting function for observations at 0.889 μm peaks at about 0.2 bars, while that for 0.727 μm peaks at about 2 bars (in the absence of scatterers). The 0.756 μm continuum channel is effectively free of methane absorption and could sense all the way down to the 38-bar level or deeper in the absence of clouds or haze, according to the equation for Rayleigh optical depth given above.

Image mosaics were obtained of spatially limited regions in several viewing angles, while the selected region rotated under the spacecraft. These so-called feature tracks were scattered between the Great Red Spot, white ovals, belts, zones, jets, hot spots, and polar regions with several of them observed more than once. With a typical spatial resolution of about 30 km/pixel, mosaics covered 20 000–30 000 km on a side. For an example of images from the first 4 feature tracks, see Vasavada *et al.* (1998).

Cloud structure modeling from *Galileo* SSI data has been discussed by Banfield *et al.* (1998b), Gierasch *et al.* (2000), and Simon-Miller *et al.* (2001b). The model was for-

mulated with at least 3 layers, corresponding to the stratosphere, upper troposphere and lower troposphere (see upper left of Figure 5.8). If necessary, multiple layers could be added anywhere, but were only ever needed in the lower troposphere. The aerosols are defined by a mean size, a single scattering albedo at 0.410 μm and an optical depth at 0.756 μm . Optical depths at the other wavelengths were calculated assuming that the aerosols were spheres of ammonia. The particles are assumed to be conservative scatterers in the near infrared. Typically, the three different aerosol layers were contiguous, with no clearings in between, but this was not forced by the structure of the model. Rarely, a second layer of lower tropospheric discrete clouds was needed to account for anomalously high near-infrared continuum (0.756 μm) channel reflectivity. Typical optical depths for the stratosphere were about 0.07, while those for the upper troposphere were about 3–7. The interface between the denser upper troposphere haze and the rarefied stratospheric haze typically fell between about 100–350 mbar.

Abundant small-scale (~ 30 km) variations in reflectivity can be exploited to extract information about the cause of those variations. Successful models of these small-scale variations in reflectivity require local changes in the condensation cloud optical thickness, in much the same way that clouds vary on Earth. An example of this is shown on the lower half of Figure 5.8. The images from which Figure 5.8 is derived are part of the paper by Vasavada *et al.* (1998). From analysis of the slopes of small-scale reflectivities plotted in color space (using coordinates in the near-IR continuum and two methane bands) Banfield *et al.* (1998b) derived condensation clouds between 600 and 950 mbar, with some extreme cases, extending as high as 450 mbar. Other extreme cases, discussed below, were found with condensation clouds at least as deep as 3 bars.

As mentioned above, the typical cloud structure found in these investigations is largely consistent with that from West *et al.* (1986). There was a thin, diffuse stratospheric haze with optical depth of about 0.05 to 0.1, particle sizes of roughly 0.01 to 0.05 μm and extending down to a pressure of between 100 mbar and 350 mbar. The upper troposphere is well fit by a thicker diffuse haze, with optical depths between 2 and 7, particle sizes of 0.6 to 1.2 μm , single scattering albedos at 0.410 μm between 0.9 and 1.0, and bottom pressures between 600 mbar and 900 mbar. Below these, optically thick, physically thin clouds were typically found at the bottom of the upper tropospheric haze, i.e., between 600 mbar and 900 mbar. In these clouds, the 0.410 μm single scattering albedos were harder to constrain but values near or equal to 1.0 are consistent with the data. Particle sizes are also poorly constrained, but sizes of order 0.9 to 3.0 μm are typical. Of course, these values are only rough estimates of what a “typical” region on Jupiter might look like, and it is clear from the *Galileo* data that horizontal variations are significant. Significant variations were found in the optical thicknesses of the lower tropospheric clouds, which varied from 0 (e.g., in hot spots) to well over 20 or more in the bright zones. Small-scale ($\sim \mathcal{O}(30$ km)) variations in these optical depths of 30% or more are also typical. Significant variation was also found in the interface between the upper and lower troposphere, where the thick condensation clouds occur. Finally, some very deep clouds (deeper than 3 bars

or more), unattached to the upper tropospheric hazes, were identified.

A specific example from the first *Galileo* orbit is a cloud structure retrieval for the middle of the Great Red Spot, and an anomalously deep cloud just to the north of the hot spots observed in the fourth orbit. Figure 5.8 shows the fit to the center of the GRS. The upper left panel shows two model schematics with pressure as the vertical coordinate and cross hatching to indicate cloud density. The single scattering albedo (at 0.410 μm), optical depth (at 0.756 μm) and mean particle size are indicated for each cloud layer. The only difference between models A and B is the optical depth of the lowest cloud layer, the lower tropospheric sheet cloud at about 530 mbar. The upper right panel shows the quality of the fit for the 4 wavelengths over the three different emission angle sets at which they were observed. The abscissa, $\mu_e = 1/(1/\mu_0 + 1/\mu)$, is representative of the cosine of the zenith angles of the combined incoming and outgoing path lengths. Small values of μ_e correspond to oblique views. The ordinate, which is the reflectivity divided by the cosine of the incidence angle, would be a constant for a Lambertian reflector without overlying absorption. Plotting the reflectivity data in this manner simplifies the behavior to almost falling along straight lines for each wavelength. This panel then shows the accord between the average of the models shown in the first panel and the average of the data for this location. The typical χ^2_ν for these fits are well under 1. The lower left panel is then simply the reflectivity in 0.756 μm plotted versus the reflectivity in both 0.727 μm and 0.889 μm for both the two models (with varying lower tropospheric sheet cloud) and a cluster of data points surrounding a point in the center of the GRS. There is a well defined slope to many of the clusters of points, which is what we have tried to match with the variations between models A and B, by tuning the level of the varying sheet cloud. The slopes in the data clusters and those between the two models match quite well, for the three 0.756–0.727 μm clusters as well as the three 0.756–0.889 μm clusters. There is a slight mismatch between the overall levels for the two brighter 756–727 clusters, but these are near the calibration uncertainties of the data, and may be due to phase function modeling errors. Finally, the lower right panel shows the cluster slopes for the 0.756–0.410 μm comparison. These also match quite well between model and data, giving further confidence in the representativeness of this model to the GRS structure. Not surprisingly, this fit for the GRS shows thick upper and lower tropospheric clouds, a relatively high interface between the upper and lower troposphere, and most strikingly, very dark particles at 0.410 μm in the upper troposphere and stratosphere, giving the spot its red color.

Many more examples of derived cloud structures can be found in Banfield *et al.* (1998b). Here we show a region of anomalous 0.756 μm reflectivity and nearby high clouds, similar to the thunderstorms discussed in Banfield *et al.* (1998b), Gierasch *et al.* (2000) and Ingersoll *et al.* (2000). This region was examined by Roos-Serote *et al.* (1998) using NIMS data, and was found to have anomalously high water-vapor abundance. Banfield *et al.* (1998b) found it to have deep clouds, at pressures greater than about 2.75 bars, indicative of water condensation clouds. Figure 5.9 shows the region, with the southern edge of the map at 10.6° N and the northern edge at 15.7° N, planetographic latitude. The

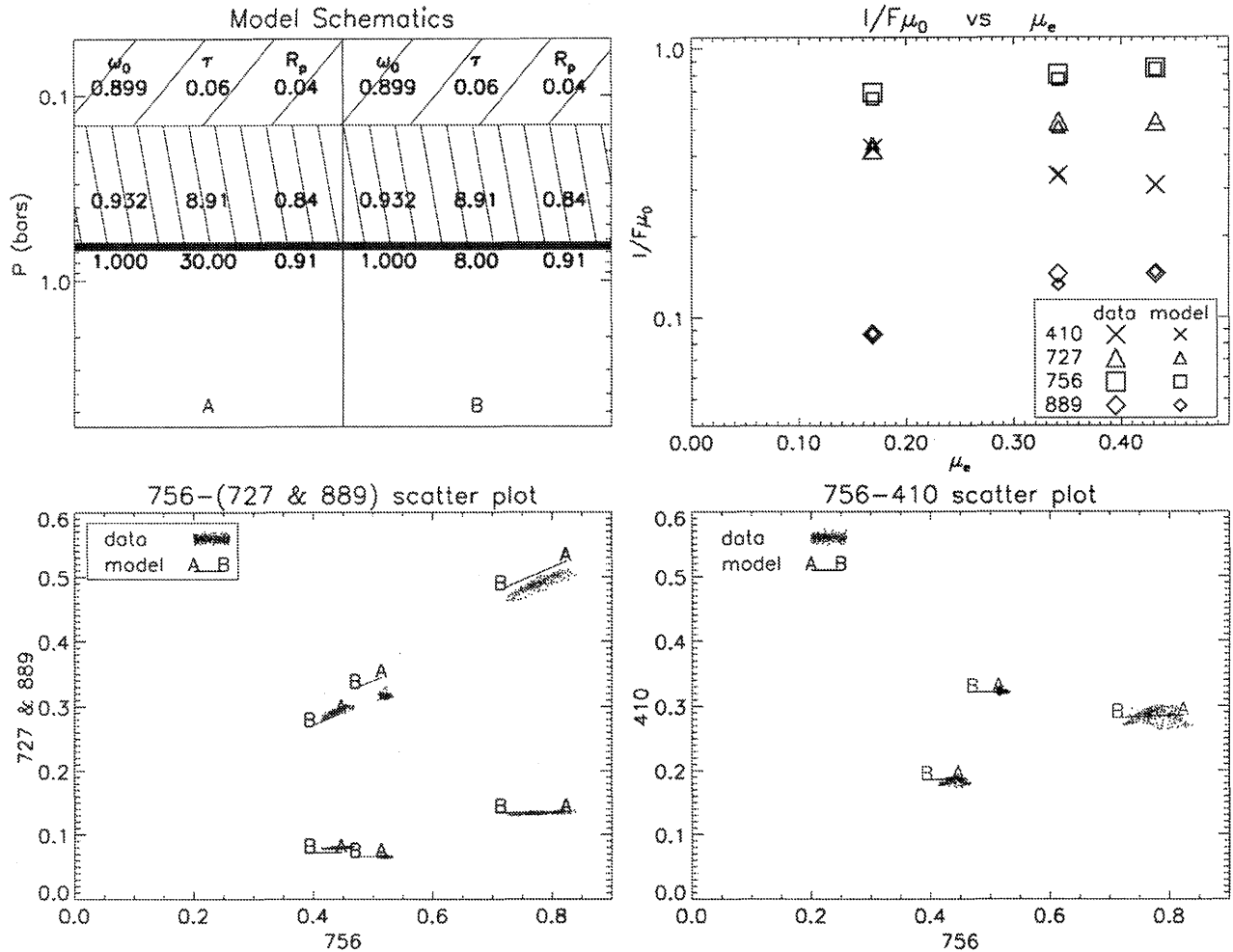


Figure 5.8. This figure illustrates how observed quantities in the *Galileo* SSI images are used to constrain parameters of the model, in this case for a region near the GRS center. The upper left panel shows two end member model structures capturing the main character of small-scale brightness variations in this region. Pressure is the vertical coordinate, hatched regions represent cloud layers. A cloud sheet sits below them at about 650 mbar. Single scattering albedo at 410 nm, 756 nm optical depth and mean particle size for each cloud layer are indicated on the plot. The two models only differ in the optical depth of the bottom cloud sheet. The upper right panel shows the match between model and data in the four wavelengths as the observing geometry changes. Small values of the ordinate μ_e represent oblique incidence and/or emission angles. The χ^2 of this fit is well below 1.0. The lower left panel shows the fit in 756 nm I/F versus 727 nm I/F and 889 nm I/F (where I is the reflected intensity and πF is the incident solar flux) between the two end member models and the local variations in the data. The six clusters are from images at three different viewing angles and two wavelengths. The slope of the cluster of data points is a strong indicator of the depth where the local variations are occurring. The lower right panel is similar to the lower left, but shows the 756 nm versus 410 nm I/F match between data and models. The flat slope on this plot suggests that single scattering albedo changes are not occurring on these small scales. Using the reflectivity variations versus μ_e , as well as matching the scatter plot slopes, we can constrain the cloud pressures to within about 20%, the 410 nm single scattering albedos to about 0.02, the 756 nm optical thicknesses to a factor of about 1.3, and the particle sizes to within a factor of about 1.5 (depending on size).

image covers an area of about $12460 \text{ km} \times 6230 \text{ km}$. The top gray-scale image is the reflectivity at $0.756 \mu\text{m}$, the middle gray-scale image is the reflectivity at $0.727 \mu\text{m}$, and the bottom image is the ratio of the two ($0.756/0.727$). Deep clouds appear bright. The storm's most active region is in the western half of the image, but the eastern half also shows evidence of deep and high clouds. The deepest cloud tops were found at the periphery of the storm. In particular the northeast corner of the western half of the storm and several spots along the southern edge of the storm all showed deep cloud tops of about 3 bars or more.

While the typical vertical structure inferred from the *Galileo* imaging-based models is very consistent with the

earlier picture from the West *et al.* (1986) review, an important new result is the discovery of deep clouds. These can only be water condensation, as ammonia or ammonium hydrosulfide would not condense at the temperatures at those levels. Interestingly, these deep clouds have been found in the vicinity of towering clouds, sticking up well into the stable region of the upper troposphere at 450 mbar. Additionally, nighttime observations of these same regions with towering clouds and deep water cloud bases reveal lightning. Porco *et al.* (2003) discuss these features as seen by the *Cassini* ISS narrow angle camera and present statistics of occurrence as a function of latitude. Ingersoll *et al.* (2000) suggested that

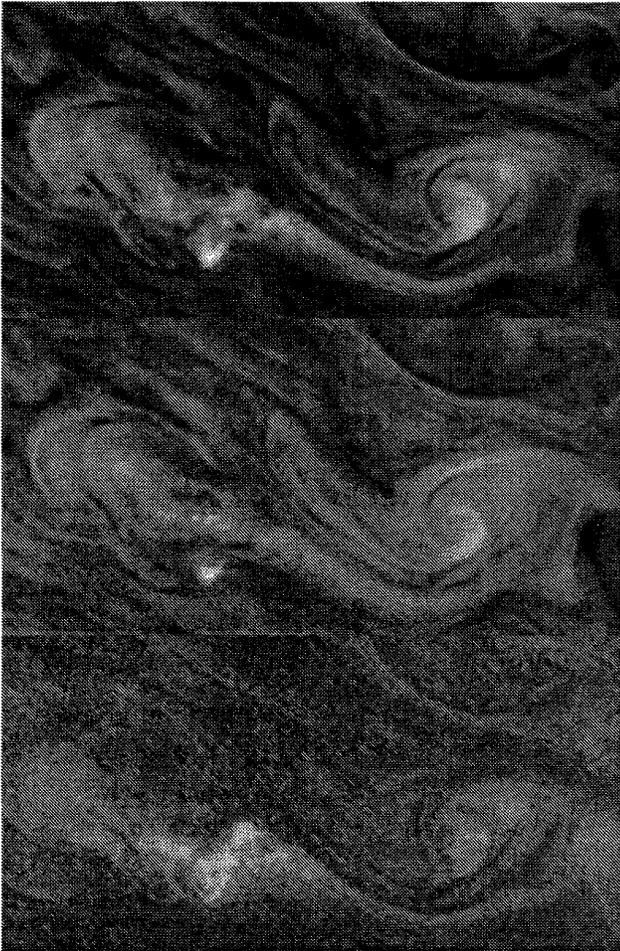


Figure 5.9. 756 nm and 727 nm views of a thunderstorm. This image covers 10.6° N to 15.7° N planetographic, an area of 12 460 km by 6230 km, just north of a hot spot. It was reported as having anomalously high water vapor amounts by Roos-Serote *et al.* (2000). The top frame is in 756 nm and senses deep and shallow clouds. The middle frame is in 727 nm and only senses shallow clouds (at pressure less than several bars). The bottom frame is the ratio 756/727 nm. Deep clouds show up as bright.

these storms may be the energy source for the motions in Jupiter's visible atmosphere.

5.2.7 Recent Analyses of Ground-Based and HST Data

Beebe *et al.* (1989) summarized what was known of the temporal variability of Jupiter's clouds and temperature fields. The North and South Equatorial Belts undergo dramatic changes in color and albedo while the zonal mean wind field remains unchanged. On smaller scales, rapid changes in cloud optical depth are apparent at $5\ \mu\text{m}$ but little variability is seen in the $0.890\text{-}\mu\text{m}$ methane band, which senses the high troposphere. West *et al.* (1986) interpreted these observations in the context of a steady-state upper tropospheric haze of small (micron to sub-micron) particles in the more stable upper troposphere overlying clouds at deeper unstable or marginally stable layers (at the base of the ammonia cloud near 700 mbar and in the ammonium hydrosulfide and

water cloud regions) composed of larger particles, opaque to $5\text{-}\mu\text{m}$ radiation.

Kuehn and Beebe (1993) used ground-based CCD images to examine the role that cloud and haze optical depth, altitude and single scattering albedo played in the dramatic increase in reflectivity of Jupiter's South Equatorial Belt (SEB) in 1989. They found that this increase in reflectivity was due mainly to an increase in the effective particle single scattering albedo of the upper tropospheric cloud, and a modest increase (from 3 to 5) of the optical depth of that cloud at visible and near-IR wavelengths. Sanchez-Lavega *et al.* (1996) provided a detailed account of the morphological changes that occurred in the SEB region in 1993 from a ground-based observing campaign.

Several investigations used ground-based and HST images in methane bands between 0.6 and $1\ \mu\text{m}$ to retrieve cloud parameters in hot spot regions after the probe results were known. Chanover *et al.* (1997) examined 31 dark regions (which are highly correlated with $5\text{-}\mu\text{m}$ hot spots) and 24 plume regions (adjacent to hot spots) in HST images. They found only slightly smaller upper-cloud optical depth in hot spot regions (6) relative to plume regions (7). These optical depths refer to a haze distributed over a pressure range of 700 to 200 mb.

Orton *et al.* (1998) combined thermal-infrared imaging at $4.78\ \mu\text{m}$ and $8.57\ \mu\text{m}$. The longer wavelength samples cloud opacity in the ammonia cloud region and higher. It is also sensitive to ammonia gas opacity, and an ammonia gas retrieval must be done independently using data at $10.74\ \mu\text{m}$. Orton *et al.* (1998) found optical depths for an upper cloud to be about half the values found by Chanover *et al.* (1997) at visible and near-infrared wavelengths. This difference can be attributed to the differing assumptions about the altitude/pressure extent of the ammonia cloud/haze which was taken to span the region between 700 mbar and 300 mbar in the model of Chanover *et al.* but to be confined to a smaller range by Orton *et al.*

The nominal cloud model proposed by Orton *et al.* includes a large-particle cloud located near the base of the ammonia cloud and an ammonium hydrosulfide cloud. Optical depths at 8.57 and $4.78\ \mu\text{m}$ (the shorter wavelength applies to the NH_4SH cloud) are 0.0 and 1.2, respectively in the middle of a hot spot. These values are in good agreement with probe results.

Sromovsky and Fry (2002) also interpreted HST images and found that the upper NH_3 cloud has a smaller optical depth (~ 2) in the near-infrared, consistent with the value found by the probe Net Flux Radiometer. These smaller optical depths are able to fit the strong methane band at $0.89\ \mu\text{m}$ if the upper haze is confined to higher altitudes (pressures in the range 240–320 mbar) rather than spread throughout the region 200–700 mbar. West *et al.* (1986, see Figure 5 of that paper) noted this same correlation in model parameters. In the Sromovsky and Fry models there is a gap in cloud density in what is normally considered the lower part of the ammonia cloud (400–700 mbar). Sromovsky and Fry argued that the vast majority of cloud structures within the North Equatorial Belt could be modeled by a relatively thin, high haze, with variable amounts of middle cloud opacities (near 1.2 bar) to account for variations in red, near-IR and $5\text{-}\mu\text{m}$ brightness. The Sromovsky and Fry paper includes a quantitative comparison of several cloud structure models

and is a valuable source for calibration and deconvolution of HST images.

5.3 TROPOSPHERIC CLOUDS AND HAZE: OPTICAL AND PHYSICAL PROPERTIES

5.3.1 Particle Composition

Until recently there has been no spectroscopic evidence for any of the condensate ices generally thought to be abundant in Jupiter's upper troposphere. Ammonia ice absorbs in relatively narrow spectral regions near 3 μm and also in the thermal infrared at 9.4 μm and 26 μm . If particles in the 200–400 mbar region are small (as the evidence suggests) they should produce strong, narrow ($\sim 0.05 \mu\text{m}$) absorption features. Large particles ($\sim 10 \mu\text{m}$ or larger) produce more shallow features which are more difficult to detect. Irregular shape can also broaden the absorption features for surface resonance modes (Huffman and Bohren 1980). West *et al.* (1989a) calculated the shape of the 9.4- μm peak for small NH_3 ice spheres and tetrahedra to see if irregular shape could account for the absence of a feature at 9.4 micron in the *Voyager* IRIS data. They concluded that the abundant small particle population in the upper troposphere could not be composed mainly of ammonia ice. The 9.4- μm feature was recently found in *Cassini* CIRS spectra but only in restricted latitude bands (M.H. Wong *et al.* 2004). The sub-micron haze in the upper troposphere (at pressures less than 500 mbar) at most latitudes does not produce an ammonia ice signature at 9.4 microns, implicating some unidentified component. The most likely candidate is N_2H_4 (hydrazine) ice produced photochemically from ammonia, but that material also has N–H stretch bonds giving rise to spectral features at nearly the same wavelength as those for NH_3 ice. A more thorough study needs to be done. Hydrazine ice has not been identified spectroscopically.

The first spectroscopic detection of ammonia ice was reported by Brooke *et al.* (1998) who noted an anomalous absorption feature in 3- μm spectra obtained by the Infrared Space Observatory (ISO). ISO's Short Wavelength Spectrometer was used to obtain a spectrum averaged over a quarter of the jovian disk, spanning latitudes from -36° to $+36^\circ$. Anomalous absorption was observed in the moderate resolution ($\lambda/\Delta\lambda \sim 1700$) spectra in the 2.7–3.2 μm range, corresponding to ammonia ice particles with a bimodal size distribution centered at 1 μm and 10 μm radii. The 10- μm particles need to dominate the 3- μm opacity in order to produce the broad, shallow feature.

Constraints on the spatial distribution, size, and age characteristics of *spectrally identified* ammonia ice clouds were reported by Baines *et al.* (2002) utilizing spectral maps from *Galileo*/NIMS shown in Figure 5.10. In Figure 5.10 the gas absorption spectrum is derived using ammonia gas coefficients from Guelachvili *et al.* (1989), Urban *et al.* (1989) and Brown and Margolis (1996). The ammonia ice spectrum is calculated from the solid NH_3 absorption coefficients of Sill *et al.* (1980). Beer's law was used to adjust the modeled gas and ice spectra to match features in the observed spectrum. Specifically, the ice spectrum (yellow) matches the observed relative reflectivity (blue) at 2.74 μm and the gas spectrum (pink) fits the general shape of the observed 1.5- μm absorption feature.

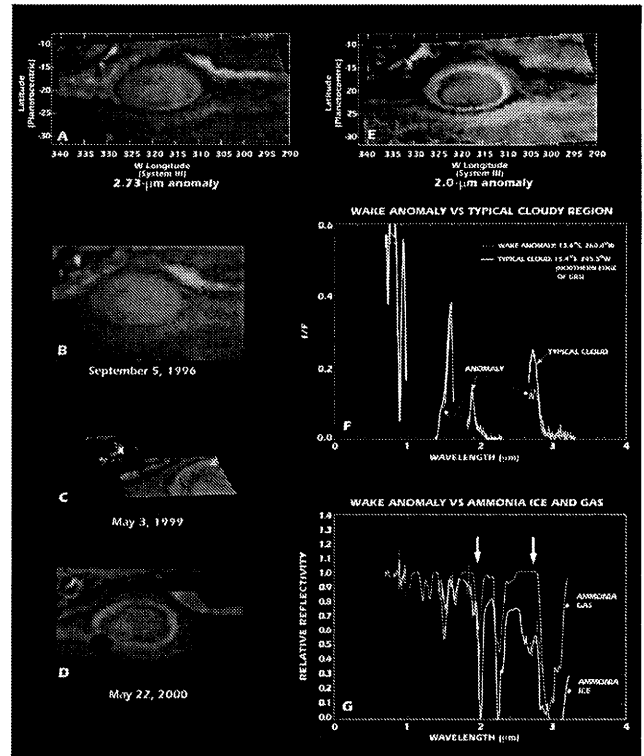


Figure 5.10. Representative images and spectra of the turbulent wake region northwest of the Great Red Spot, showing spectroscopically-identifiable ammonia clouds from Baines *et al.* (2002). Color renditions of *Galileo* NIMS images acquired during the first four years of Jupiter reconnaissance are shown in Panels A–E. On the left (Panels A–D), red denotes high reflectivity at 1.6 μm , indicative of optically thick clouds, blue denotes areas of high 5- μm flux transmitted through essentially clear atmospheric regions, and green denotes regions of low 2.73- μm reflectivity. The X symbols in Panel C give locations of spectra plotted in Panels F and G. The turbulent wake region is yellow, indicating a cloudy region of high 1.6- μm opacity and large 2.73- μm absorptivity indicative of ammonia ice absorption. In Panel E (top right), this feature appears a pale color, indicative of a cloudy region of high 1.6- μm opacity (green) at high altitude (red, showing reflectivity in the highly absorbing 2.05- μm hydrogen feature) and low 1.99- μm absorption (blue, showing high 1.94- μm /1.99- μm band depth, indicative of strong ammonia absorption). The core of the Great Red Spot itself appears orange, indicative of its high altitude and high reflectivity. Surrounding it is a yellowish region showing a ring of material at slightly lower altitudes. A spectrum (blue curve in Panel F) acquired of an anomalous feature on May 3, 1999 shows both the 1.99- μm and 2.73- μm absorptions compared to the high reflectivity seen in a nearby cloud of comparable altitude (yellow). The ratio of these two spectra is shown as the blue spectrum in Panel G. This normalized spectrum effectively eliminates spectral artifacts due to overlying well-mixed gases such as hydrogen and methane. The resulting spectrum correlates well with ammonia ice (yellow) but not ammonia gas (pink), especially near 2.7 μm (right arrow) where ammonia gas does not absorb. Images acquired throughout the first four years of the *Galileo* reconnaissance (Panels A–D) indicate that such spectroscopically-identifiable ammonia ice clouds occur frequently in the turbulent wake region northwest of the Great Red Spot. At the time of going to press a colour version of this figure was available for download from <http://www.cambridge.org/9780521035453>.

Examining a global image set, Baines *et al.* (2002) found that these ammonia clouds were rather small in size (less than three degrees in latitude and longitude in most cases) and covered less than 0.5% of the planet. The most prominent features seem to be associated with regions of strong vertical transport. More than half of the most spectrally-prominent clouds reside within a small latitudinal band from 2–7° N, just south of the 5- μ m hot spots. The longitudes of these cloud features are correlated with the longitudes of hot spots, indicating that both types of features are associated with a common planetary wave, such as an equatorially trapped Rossby wave previously suggested by Allison (1990) and Ortiz *et al.* (1998) to explain the semi-regular longitudinal distribution of hot spots. Recent quantitative dynamic modeling (Showman and Dowling 2000, Friedson 2002b) supports this picture. These models are surprisingly consistent with a number of unexpected *Galileo* probe and *Galileo* NIMS results, including the wide spatial variability in the abundances of condensables as well as the steep vertical gradient in the zonal wind speed measured by the *Galileo* probe (Atkinson *et al.* 1998). The Showman and Dowling (2000) nonlinear analysis in three dimensions predicts that isentropes at depth in the hot spots should rise to much lower pressure at more southerly latitudes between hot spots, consistent with the Baines *et al.* (2002) measurements of upper-tropospheric ammonia ice condensation at such locations.

The most spectrally-prominent ammonia ice feature on the globe is found in the turbulent wake region northwest of the Great Red Spot. *Galileo* NIMS measurements over a four-year period consistently found a prominent ammonia ice cloud centered 10–15 degrees north and 10–20 degrees west of the center of the Great Red Spot (Baines *et al.* 2002), nearly tangential to the perimeter of the Great Red Spot. The feature typically extends some 6000 km by 1000 km, with the long axis oriented in the northeast–southwest direction. A streamline analysis, assuming that ammonia ice is created in a semi-standing wave at the head of the feature and are then swept downstream by ~ 60 m s⁻¹ winds, consistent with the zonal winds measured at the northern and southern ends of the feature (Limaye *et al.* 1986), indicates that ice particles survive for just 1–2 days. A similar particle age is found for ice clouds associated with hot spots, as calculated from the Rossby wave phase speed of 41 m s⁻¹ reported by Ortiz *et al.* (1998). Thus, ammonia ice particles are remarkably young, living for only a short time in a spectroscopically-identifiable state in the jovian atmosphere.

Water clouds have also been recently identified spectroscopically in Jupiter's atmosphere. Using *Voyager* IRIS spectra near 44 μ m, Simon-Miller *et al.* (2000) reported possible signatures of water ice in approximately 1% of IRIS spectra. As with the ammonia ice, these detections were clustered near the Great Red Spot and 5- μ m hot spots, as well as other regions with suspected strong vertical motion. About 1 precipitable micron of water with 2- μ m radii Mie scattering particles fit the spectra.

5.3.2 Particle Optical Properties, Size and Shape

Particle optical properties (scattering phase function, polarization and absorption and scattering cross sections) and their wavelength dependencies can provide valuable clues to

the size, shape and composition of particles. Retrievals of cloud and haze optical depth depend on these properties. So do estimates of radiative heating and cooling. For these reasons it is important to obtain accurate information on particle optical properties.

At the cold temperatures of the upper troposphere, condensates of ammonia, ammonium hydrosulfide and water would be in the ice phase except for a portion of a deep water-ammonia solution cloud that may be in the liquid phase. For this reason we do not expect to see evidence for spheres (such as rainbows) and none have been observed. Scattering phase functions for spheres whose radius is comparable to or larger than the wavelength generally have a deep minimum between 90 and 120 degrees scattering angle that is not seen in phase functions for non-spheres, and the strong glory (the narrow peak in the back-scattering direction) is muted for non-spherical shapes. Mie theory for spheres has been used for retrievals because computations can be made easily for a large variety of sizes and refractive indices. The results of these retrievals must be scrutinized to verify that they are insensitive to the assumption of spherical shape. Limb darkening at low phase angles is especially sensitive to the shape of the scattering phase function of the top-most aerosol layer.

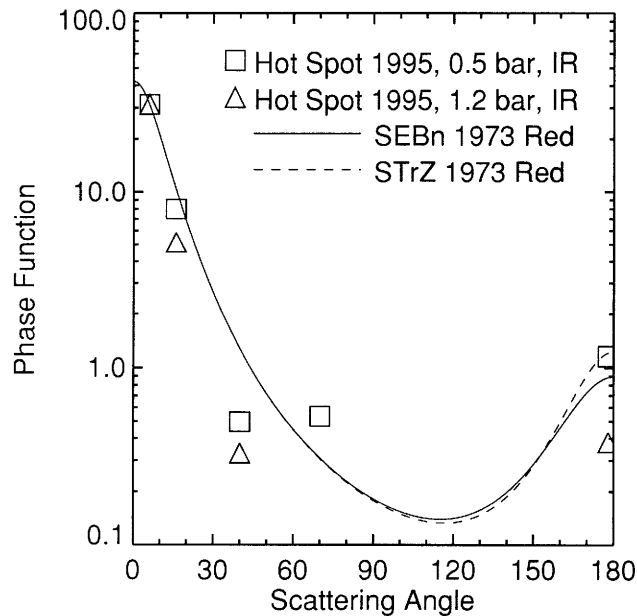
The Imaging Photopolarimeter on the *Pioneer 10* and *11* spacecraft provided the first photometric and polarimetric measurements of Jupiter at large phase angles. Phase functions derived by Tomasko *et al.* (1978) from these data are still used for radiative transfer models of Jupiter's clouds and haze because no other spacecraft has obtained a data set with as complete coverage in phase angle. Measurements from the *Galileo* orbiter instruments and instruments on the *Cassini* spacecraft sample wavelengths and times not available to the *Pioneer* spacecraft and *Galileo* probe Nephelometer. Analyses of these data are pending and should add important knowledge when completed. The *Galileo* probe Nephelometer provided the only in situ measurements of particle phase functions.

Tomasko *et al.* (1978) derived phase functions described by a double Henyey–Greenstein formalism, $P(g_1, g_2, f, \theta) = fP_{HG}(g_1, \theta) + (1 - f)P_{HG}(g_2, \theta)$, where $P_{HG}(g, \theta) = (1 - g^2)/(1 + g^2 - 2g \cos \theta)^{3/2}$ is the Henyey–Greenstein function whose asymmetry parameter is g and θ is the scattering angle. The g_2 parameter is negative and accounts for a back-scattering peak. The parameters that best fit the *Pioneer* observations are given in Table 5.2.

The phase functions for belt and zone particles are similar. Tomasko *et al.* attributed the difference in albedo mainly to a difference in the single scattering albedo of the cloud and haze particles in the upper troposphere. Banfield *et al.* (1998b) and Sromovsky and Fry (2002) argue that albedo contrasts at near-infrared wavelengths are caused by optical depth variations in condensate clouds that overlie absorbing material in the deeper atmosphere. A resolution of these competing views is a goal for future research. Doose *et al.* (1986) extended the analysis of *Pioneer* data to other latitudes. They found that tropospheric phase functions for mid-latitude regions are similar to those derived for the north component of the South Equatorial Belt (SEBn) and the South Tropical Zone (STrZ). At high latitudes a different phase function is needed because the stratospheric haze becomes optically thick at ultraviolet and visible wave-

Table 5.2. Parameters of the best-fit double Henyey–Greenstein phase functions for tropospheric aerosols. Values are from Tomasko *et al.* (1978) for their Type II models.

Region	Blue ($\lambda = 0.44 \mu\text{m}$)				Red ($\lambda = 0.64 \mu\text{m}$)			
	g_1	g_2	f	ω	g_1	g_2	f	ω
SEBn	0.80	-0.75	0.979	0.970	0.80	-0.65	0.938	0.991
STrZ	0.80	-0.80	0.969	0.995	0.80	-0.70	0.938	0.997
Stratosphere	0.75	0.0	1.0	>0.95	0.75	0.0	1.0	>0.95

**Figure 5.11.** Particle scattering phase functions at $0.64 \mu\text{m}$ derived for Jupiter's upper troposphere from 1973 *Pioneer 10* data (Tomasko *et al.* 1978) and 1995 measurements at $0.904 \mu\text{m}$ from the *Galileo* probe Nephelometer (Ragent *et al.* 1998). The Nephelometer measurements were normalized to the same value as the *Pioneer*-derived double Henyey–Greenstein functions at a scattering angle of 5.8 degrees.

lengths, and this haze has very different physical characteristics, which will be discussed in the section on stratospheric aerosol.

The *Galileo* probe Nephelometer measured intensities at five angles, 5.8° , 16° , 40° , 70° , and 178° at a wavelength of $0.904 \mu\text{m}$. As Figure 5.11 shows, these and the double Henyey–Greenstein phase functions derived by Tomasko *et al.* (1978) for the red SEBn are in good agreement for the 0.44 -bar region, but the Nephelometer measurements at 1.24 bars are more strongly peaked at small scattering angles. The more strongly peaked phase function is indicative of larger particles (several microns radius, according to Ragent *et al.* 1998).

The probe Net Flux Radiometer observed a spin-modulated signal (due to probe rotation) in short-wave (solar) channels (Sromovsky *et al.* 1998). The amplitude of the modulation and wavelength dependence are best fit by sub-micron particles (radii 0.5 – $0.75 \mu\text{m}$) at pressures less than 0.5 bar. The deeper cloud layer sensed by the Nephelometer is consistent with particles having mean radii between 3 and $5 \mu\text{m}$. These values are in turn consistent with the

picture presented by West *et al.* (1986) for hot spot regions, although the middle cloud is elevated above the base level of the NH_4SH cloud in the solar-composition thermochemical equilibrium model. Gierasch *et al.* (1986) reported similar results from analyses of *Voyager* IRIS data at 5 and $45 \mu\text{m}$, but identified the large-particle component as being near the base of the ammonia cloud.

Particle polarization can be a diagnostic of particle size and refractive index, although for non-spherical ice crystals only a limited interpretation is possible. Smith and Tomasko (1984) found that two very different types of particles are apparent in polarization images of Jupiter. At low latitudes the upper tropospheric haze is only very weakly polarizing in both blue and red wavelengths, and slightly negatively polarizing at red wavelengths (negative linear polarization has the electric vector oscillating in the scattering plane). At high latitudes the particles are strongly positively polarizing. The weak or negatively polarizing particles have effective radii comparable to or larger than the visible wavelength, while the strongly polarizing particles are either small or aggregates of small particles. West and Smith (1991) favor aggregates of small particles because moderately strong forward scattering is also observed. In order to fit the center-to-limb behavior of the polarization, Smith and Tomasko proposed an optically thin ($\tau \sim 0.1$) layer of small positively polarizing particles above the weak negatively polarizing particles. This layer corresponds to a thin stratospheric haze discussed below.

The *Galileo* orbiter Photopolarimeter Radiometer (PPR) measured linear polarization in a blue and red filter and also in a near-infrared filter at $0.94 \mu\text{m}$. According to Braak *et al.* (2002) the main polarization features mentioned above from the *Pioneer* studies were present also in the *Galileo* data, although the particles at low latitudes were more negatively polarizing at the time of the *Galileo* observations (May and June of 1997, 23 years after the *Pioneer 10* and *11* observations).

Laboratory studies of the polarizing properties of ammonia ice particles were undertaken by Pope *et al.* (1992). Temperature and the degree of saturation are the main factors which controlled particle size and shape in their cloud chamber experiment. Octahedra and tetrahedra are the principal shapes predicted from molecular symmetry. Some of the crystals produced in the chamber were in this form but most had irregular shapes. The polarization observed from Jupiter's upper tropospheric cloud is weakly negatively polarizing and changes little with wavelength. These characteristics indicate particles whose size parameter ($2\pi r/\lambda$) is between about 5 and 20 . The corresponding effective particle radius is in the range 0.5 to $2 \mu\text{m}$. The smaller end of this range is consistent with particle size in the up-

per troposphere determined from other data discussed previously. Larger particles are more negatively polarizing. It is possible that the stronger negative polarization observed by the *Galileo* PPR is indicative of an enhancement in the large particle part of the size distribution.

Halo features near 43 degrees scattering angle predicted for ammonia tetrahedra and octahedra at larger size parameters are not seen in laboratory measurements and could not be observed in the *Pioneer* or *Galileo* data because the phase angle sampling was not sufficiently dense. Polarization for these shapes is positive in the scattering angle range 60° to 100° (phase angles between 80° and 120°). In the terrestrial cirrus, regularly shaped ice crystals are in the minority and for that reason halo features in cirrus clouds are seen only about 20% of the time.

5.3.3 Chromophores

Jupiter's geometric albedo spectrum at moderate spectral resolution (see Karkoschka 1998) can be explained by gaseous methane and ammonia and a particulate whose absorption increases gradually and monotonically from red to blue (see Figure 5.3). Minimum albedo at short wavelengths is near 0.3 μm in the near-UV.

All of the ices predicted from thermochemical equilibrium models are white at visible wavelengths. The composition of coloring agents continues to be a major unresolved question. Table 5.3 lists candidates which have been proposed and laboratory measurements of spectral properties. Some combination of photochemistry and lightning discharge is thought to produce non-equilibrium molecules involving S, C and N atoms. It is likely that at least one of the candidates in Table 5.3 is responsible for the coloration, but the problem is that few of them can be ruled out on the basis of observation. There are no narrow, distinguishing spectral features which could identify one candidate. Various authors have argued in favor of one hypothesis over another based on energetics or stability and these comments are noted in the table. These are essentially the same conclusions that Sill (1976) came to in his synthesis of the field more than 25 years ago.

Smith and Tomasko (1984) and Simon-Miller *et al.* (2001b) showed that colored material resides in the ammonia haze region. Smith and Tomasko argued that coloration is present also in a deeper cloud, but Simon-Miller *et al.* (2001b) confine the colored material to the ammonia haze region, above the base of the ammonia cloud. In the model of Simon-Miller *et al.* the underlying ammonia sheet cloud (at the base of the ammonia cloud layer) is white.

Simon-Miller *et al.* (2001a) performed a principal-components color analysis of HST images at several wavelengths. The derived components describe departures from the mean albedo of Jupiter, which is highest in the red. Ninety-one percent of albedo variation on Jupiter are due to spectrally neutral variations; another 8% of the variation is due to a red component. The Great Red Spot's spectrum is significantly redder than other regions due to enhanced absorption at blue wavelengths. Some smaller red spots share this attribute (Beebe and Hockey 1986). The GRS shows strong contrast in the second component, and has a signature in the third (1% of the variance) component, as do some, but not all, smaller anticyclonic ovals. With the lim-

itations of PCA and the few wavelengths used, the significance and spectral nature of the third component is not yet understood.

The 91% of variation attributable to a spectrally neutral component, coupled with observations that some belt regions can change albedo on short timescales with little change in temperature or wind field, suggests that colored particles may be ubiquitous in the high troposphere and that small changes in saturation conditions may lead to condensation of white ammonia ice or hydrazine on to less volatile chromophore condensation nuclei. This may be occurring on small spatial and timescales but also during times when a large region of the SEB brightens and becomes zone-like in appearance.

5.4 STRATOSPHERIC HAZE

5.4.1 Particle Distribution, Optical Properties, Size and Shape

The earliest indications that aerosols are an important component of Jupiter's stratosphere came from measurements of Jupiter's geometric albedo in the near-ultraviolet (Axel 1972). Jupiter's albedo is lower than expected at UV wavelengths for a clean H₂-He atmosphere with a trace amount of ammonia gas. In the early years (before 1980) the stratospheric haze became known as "Axel dust", and later as "Axel-Danielson dust" in tribute to contributions by the late Robert Danielson of Princeton University. These early UV observations did not have sufficient spatial resolution to indicate that the haze is concentrated at high latitudes. Images in strong methane bands obtained before 1970 did show a polar haze (Owen and Mason 1969, Minton 1972) but it was not realized until many years later that the aerosols producing the high reflectivity were located at altitudes well above the tropopause level.

Stratospheric haze at low and middle latitudes (between -55° and +35°) is optically thin. Optical depth derived from satellite eclipse observations at 1.05 μm is less than 0.07 (Smith 1980). Models of limb darkening and phase behavior from *Pioneer 10* (Tomasko *et al.* 1978) and from ground-based (West and Tomasko 1980) and HST images (Sromovsky and Fry 2002) cluster at values between 0.2 and 0.35 in the wavelength range 0.6 to 0.95 μm . Sromovsky and Fry proposed that the wavelength dependence in this region (increasing optical depth with wavelength) implies a mean radius near 0.5 μm with a very narrow size distribution. A better estimate of particle mean radius comes from consideration of a broader spectral range. Tomasko *et al.* (1986) found that particles with mean radii in the range 0.2-0.5 μm were required to fit derived optical depths over the wavelength range 0.22 to about 1 μm . This range includes the range of values favored by Sromovsky and Fry, but particles as large as 0.5 μm would have an optical depth at 1.05 μm comparable to their value at 0.953 μm . It seems unlikely that any model can accommodate optical depths derived from methane band and continuum images (~0.3) with the much smaller optical depths at a slightly longer wavelength derived from satellite eclipse data.

Two other observational constraints can be applied to determine particle mean radius and optical depth. The un-

derlying ammonia or hydrazine haze in Jupiter's upper troposphere is negatively polarizing but the center-to-limb behavior of the polarization shows that the upper 0.3 optical depth of haze is positively polarizing (Smith 1986). The positive polarization suggests that the particles are smaller than the wavelength, but the details depend on particle shape. Aggregates of small particles can have large positive polarization even for relatively large effective size (West 1991). A measure which is less sensitive to particle shape is the scattering phase function at small scattering angles. Tomasko *et al.* (1978) showed that the stratospheric haze particles at low latitude are forward scattering with very little back scatter. A single Henyey–Greenstein phase function with asymmetry parameter 0.75 provided a good fit to the high phase angle observations. This requires the particles to have a mean radius that is comparable to the wavelength.

Rages *et al.* (1999) examined *Galileo* images at high phase angle. They derived vertical profiles of aerosol extinction at two wavelengths and two latitudes. At 9° planetographic latitude they found particle mean radius to decrease from 0.45 μm to 0.32 μm in the pressure range 96 to 16 mbar sensed by a near-IR and violet filter. At 60° latitude two solutions are possible, one with particles having slightly smaller radii at slightly higher pressures, and another with larger particles (0.6 to 1.3 μm) if the particle layer is in the pressure range between 1 and 2 mbar. West (1988) found smaller particles (radii less than 0.1 μm) at lower pressures (as low as 0.5 mbar) from *Voyager* images of Jupiter's limb at very high phase angle (near 177°).

The combination of modest forward scattering and moderately strong positive polarization for stratospheric haze particles cannot be easily explained by a single size distribution of spheres. A model with a thin layer (optical depth less than 0.1) of spheres overlying a larger optical depth of small polarizing particles might be able to fit both constraints but this configuration does not agree with the vertical gradient in particle size derived from measurement as described in the previous paragraph. The combined constraints are best accommodated by aggregates of small monomers whose effective radius is less than 0.1 μm but whose effective mean radius is near 0.5 μm (West and Smith 1991).

The *Galileo* images described by Rages *et al.* (1999) provide the most detailed information we have on the vertical profile of stratospheric aerosols at two latitudes. Rages *et al.* found a particle scale height similar to the gas scale height at low latitude but at 60° planetographic latitude there was a discrete haze layer seen on only one of two images separated by 20° in longitude. Evidence for the heterogeneous nature of the high-latitude aerosol was reported previously by West (1988) from analysis of *Voyager* eclipse images. We will comment further on this, but first show vertical profiles derived at lower vertical resolution but with much more complete latitude coverage from the near-infrared ground-based spectra. These were obtained by Banfield *et al.* (1998a) who applied a retrieval algorithm similar to one that has been used to retrieve temperature from spectra. The resulting retrievals shown in Figure 5.12 are not influenced by *a priori* model assumptions except for the assumption that the aerosol back-scattering has no wavelength dependence. Stam *et al.* (2001) showed how that assumption can be relaxed.

In the retrievals shown in Figure 5.12 the stratospheric

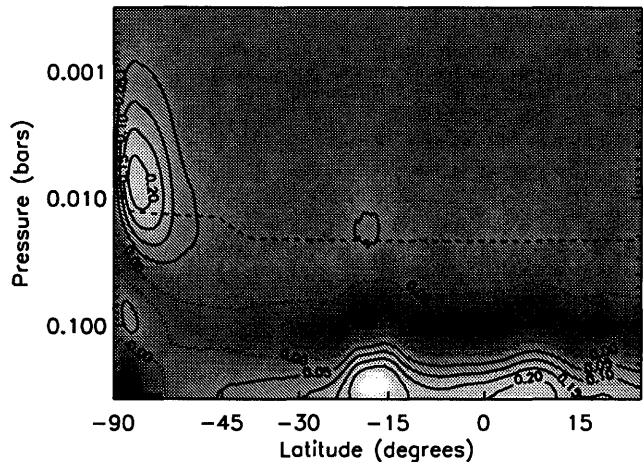


Figure 5.12. Adapted from Banfield *et al.* (1998a). Intensity observed in the strong methane bands which sample the stratosphere of Jupiter is dominated by photons scattered once from the haze particles. It is proportional to the number density of particles times the scattering phase function times the single scattering albedo times the scattering cross section. Here we call that product the mixing ratio and it has units of optical depth (dimensionless) per bar of pressure. The brighter shading indicates higher aerosol mixing ratio. The dark lines are contours of the mixing ratio, with the zero contour dotted. The dashed line represents the maximum of the highest weighting function used in the retrievals. It varies with latitude because the viewing becomes more oblique toward the poles. Above this line, the retrievals have no vertical resolution, and values should be considered as indicative of the vertically integrated aerosol load above that point. The retrievals shown here cut through the longitude of the Great Red Spot. Retrievals at other longitudes do not show the elevated upper tropospheric haze between latitudes -15° and -25° . Distance from the equator along the abscissa is proportional to $\sin(\text{latitude})$, and no data are available north of $+25^\circ$.

aerosols are distributed almost uniformly in latitude except for the concentration in the polar hood between 1 and 20 mbar pressure level, with the highest concentration near 8 mbar. This has important implications for solar heating in the stratosphere and for the residual circulation, as discussed in Chapter 7. Figure 5.12 also shows that the upper tropospheric haze is higher in the latitude range between 0 and 9 degrees rather than in the region centered on the equator that is depicted in the schematic in Figure 5.6. The retrievals also show a minimum in the aerosol mixing ratio near the tropopause. This is contrary to expectations from hydrazine photochemical models (Kaye and Strobel 1983). It suggests that hydrazine photochemistry takes place at deeper levels with little transport up to the tropopause, or that particles grow from the vapor or by coagulation and rapidly fall out of the region near the tropopause.

Jupiter's stratospheric haze becomes optically thick at high latitudes. Polarization, UV reflectivity and methane band imagery all corroborate this view. Tomasko *et al.* (1986) estimated an increase of a factor of 7 from low latitude to 40°. Rages *et al.* (1999) found an increase of this magnitude between low latitudes and 60°. Vertical optical depth at visible wavelengths is near unity in the latitude range 40°–60° if the estimates cited above for low latitudes are correct. Optical depth of the polar haze appears to increase at still higher latitude, although it is difficult to

know the magnitude of this since the view is highly foreshortened. The high-latitude concentration of stratospheric aerosols suggests that auroral destruction of methane with subsequent ion and neutral chemistry is the ultimate source of the haze material (Hord *et al.* 1979, Pryor and Hord 1991).

The onset of the stratospheric optical depth increase occurs at about 35° latitude in the north and near -55° in the south. At ultraviolet wavelengths, especially below $0.3 \mu\text{m}$, the dark stratospheric haze rapidly becomes the dominating feature and is strongly asymmetric between the hemispheres. In the south the stratosphere is relatively clear until a sharp onset poleward of -55° latitude. In the strong methane band at $0.89 \mu\text{m}$ the south polar haze appears sharply delineated and brighter than the more diffuse and weaker north polar haze. Since the longer wavelengths are more sensitive to the large end of the particle size distribution, these coupled observations argue for a population of small particles (probably less than $0.2 \mu\text{m}$ effective radius) that is abundant in the north all the way to latitude 35° , with fewer large particles relative to those in the southern polar vortex.

The north/south asymmetry is consistent with the idea that auroral energy is responsible for the existence and distribution of the haze. In the north the auroral main oval extends to lower latitudes than it does in the southern hemisphere. In addition, the aerosols must be transported to reach lower latitude, so there is an obvious coupling with atmospheric transport. The polar haze is bounded on the low-latitude perimeter by a wave pattern seen in $0.89\text{-}\mu\text{m}$ methane images and more strongly in the near-UV images. Sanchez-Lavega *et al.* (1998) pointed out the likelihood that these are Rossby waves. They provide a mechanism for latitudinal transport. The zonal jets provide a confining mechanism. Qualitatively the coupling of these with the source from the asymmetric auroral precipitation accounts for the observed latitude distribution. A detailed model for this process has yet to be developed. Recent observations described next should motivate this effort.

HST UV images taken from 1994 to 1999 and *Cassini* UV images taken in 2000 show details in the morphology and motion of the polar stratospheric haze that were hardly imagined prior to 1994. The most fruitful wavelengths have been in the range $0.20 \mu\text{m}$ – $0.29 \mu\text{m}$ where the aerosol is dark against an underlying Rayleigh scattering molecular atmosphere and yet the signal is high enough to show details at relatively short integration times. Vincent *et al.* (2000a) described the appearance of Jupiter in low and mid-latitudes. At UV wavelengths the contrast in belts and zones is not well correlated with contrast at visible wavelengths. The darker regions correspond to places where the upper troposphere haze is higher and thicker. This suggests that a UV absorber is embedded in the upper ammonia or hydrazine haze in the 200–400 mbar region. Perhaps this is a signature of hydrazine.

In UV images, wave structure is very prominent in middle/high latitudes (between latitudes 40° and 60° in the north) but is not apparent closer to the pole. Vincent *et al.* (2000b) described a number of other features seen in HST images taken between 1994 and 1997. They proposed that some of the contrast seen in the longer-wavelength UV images are fixed in System III longitude and are thus tied to or aligned with the auroras. They also estimated the zonal wind in the polar stratosphere by tracking features in 1996

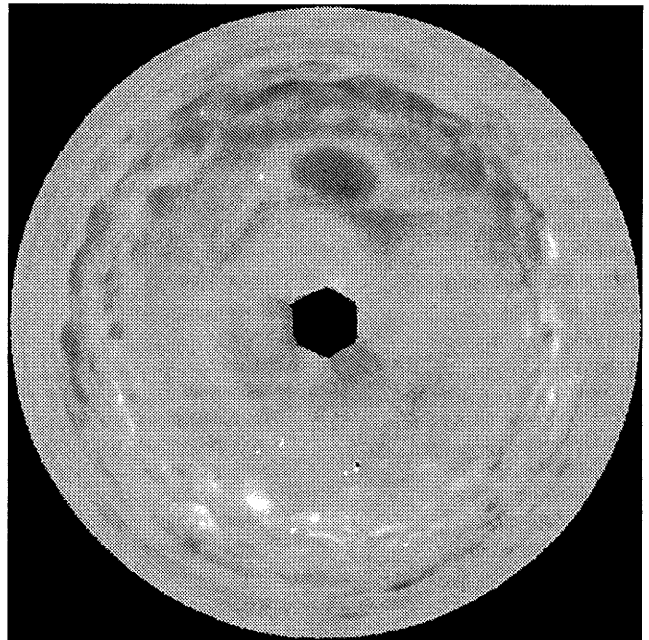


Figure 5.13. This polar-projection mosaic of Jupiter's north pole was constructed by map-projecting six HST images obtained with the F255W filter in September, 1997. Limb darkening was removed and the images were divided by a zonal mean of Jupiter's reflectivity at each latitude to show residual contrasts. System III longitude 180° is at the top of the image.

images and found that it decays with altitude as expected from previous work.

HST UV images obtained in October, 1997 revealed a large dark oval, about the same size and shape as Jupiter's Great Red Spot, and nested within the southern extent of the main auroral oval. This is shown in Figure 5.13. This feature was not seen in other images during the period 1994–1997. It disappears at longer wavelengths and is not seen in the $0.89\text{-}\mu\text{m}$ methane image taken with HST during the same time, although Dewoody *et al.* (2001) reported an enhancement in reflectivity of the polar hood seen in ground-based images. It is therefore likely that the feature is a collection of very small $\leq 0.1 \mu\text{m}$ particles. Its location and the alignment of its southern boundary with the main auroral oval suggest that an auroral process is involved, but the alignment is transient. In any case, this and other contrast features within the polar vortex can serve as tracers of vorticity and circulation much like ozone does in the terrestrial stratospheric polar vortex.

The *Cassini* ISS instrument captured the formation and part of the life cycle of another large dark oval with time-lapse photography over a 2.5-month period beginning October 1, 2000 (Porco *et al.* 2003). At the beginning of that period a diffuse dark region with about half the area of the GRS was seen to the west of the main auroral oval. After three or four weeks the dark region was more distinct, with a sharp boundary and size, shape and location in System III coordinates very similar to those for the 1997 feature shown in Figure 5.13. At this time the southern perimeter of the oval was aligned with the main auroral oval. Over the next month the oval flattened in latitude and stretched in longitude and moved out of the auroral oval to the east (prograde

flow) and a little to the south. Other, smaller features were seen in the *Cassini* UV movie (Porco *et al.* 2003). Near the end of the sequence a smaller dark region formed closer to the pole and was observed to shear and move to the west in response to the wind field. Small features were seen in the south polar region but no large oval was observed in the southern polar vortex.

5.4.2 Particle Formation

It is likely that the formation of the large oval and other features seen in the polar haze have a link to the auroral precipitation process. It is not obvious what that link is. The most compelling evidence is the location of the large dark oval within the main auroral oval at the time when the dark oval is at maximum contrast. The alignment of the southern perimeter of the dark oval with the main auroral oval during that time suggests that the auroral process is contributing to the formation of the dark material. The auroral connection is clouded by the observation that the large dark oval appears to form at least partly outside the main oval and moves outside of the oval near the end of the sequence (see Porco *et al.* 2003).

The large oval formation may be a quasi-periodic phenomenon or it may be a rare but recurring event triggered by an unusual auroral event. On timescales of weeks auroral precipitation is a nearly continuous process along the main oval, thought to be tied to plasma corotation breakdown in the middle magnetosphere (Cowley and Bunce 2001). A steady production of haze particles from this source might couple with unsteady flows in the upper atmosphere, leading to a local concentration of particles. Other magnetospheric processes produce less frequent but more intense auroral events that might play an important role. The joint *Cassini/Galileo/HST* auroral/magnetosphere campaign provided convincing evidence that fluctuations in solar wind plasma parameters perturb the jovian magnetosphere and lead to particle precipitation in a way familiar from the terrestrial experience (Waite *et al.* 2001, Gurnett *et al.* 2002, Mauk *et al.* 2002). The source region for auroral particles during these events is at great distance in the magnetosphere, which maps into an auroral footprint closer to the magnetic pole. If this mechanism were responsible for the production of dark haze we would expect to see the dark material originate closer to the pole. Porco *et al.* (2003) report that a dark feature does form at a higher latitude near the end of the *Cassini* ISS sequence, as mentioned above. Yet another mechanism produces X-ray emission, maps to higher latitude (Gladstone *et al.* 2002), and also may be a better candidate for the small dark region that is seen to form near the end of the observational period. Finally, energetic charged particle precipitation at lower latitudes is associated with the Galilean satellites, especially Io (Clarke *et al.* 2002).

Charged particle precipitation is not the only mechanism which might lead to haze formation, especially at low latitude. In early work on photochemistry, Strobel (1973) proposed that ammonia photolysis in the lower stratosphere leads to the production and condensation of hydrazine (N_2H_4). Hydrazine continues to be a candidate for haze at low latitudes (Moreno 1996). Photochemistry involving methane is also possible.

While observations indicate that polar stratospheric haze production begins with photochemical and auroral energetic breakdown of methane, our knowledge of the chemical path from methane decomposition to solid particle formation is incomplete. Pryor and Hord (1991) proposed a sequence of ion-neutral reactions leading to the formation of heavy hydrocarbon ions that might serve as the precursors to carbonaceous aerosols; however, the implications of their chemical model could not be examined in detail since the recombination products of the heavy hydrocarbon ions were unknown.

Subsequently, Wong *et al.* (2000) proposed a primarily neutral photochemical pathway to complex hydrocarbon and polycyclic aromatic hydrocarbon (PAH) formation in the auroral zones. In their model, energetic particle precipitation in the auroras accelerates the net destruction of methane, leading to greatly enhanced production of benzene, PAH and other complex hydrocarbons. They calculated a maximum volume mixing ratio of benzene that compares favorably with the value of $2_{-1}^{+2} \times 10^{-9}$ observed in the north polar region by Kim *et al.* (1985), but the associated column abundance above the 50-mbar level is a factor ~ 4 less than the $9_{-7.5}^{+4.5} \times 10^{14}$ cm^{-2} derived by Bézard *et al.* (2001) from ISO data. Two-, three-, and four-ring PAH compounds were predicted to be saturated with respect to their vapors at various altitudes.

The idea that PAH synthesis occurs in the auroral zones is appealing. PAHs are important molecular precursors of soot particle nucleation in laboratory combustion experiments (Richter and Howard 2000) and it is tempting to think that they may also be important precursors of jovian polar haze formation. Different physical processes would have to be responsible for gas-to-particle conversion in these very different environments, however. In laboratory combustion, soot particles are thought to nucleate through a complex process involving high-temperature polymerization of heavy PAH species, whereas for the jovian auroras, the model of Wong *et al.* (2000) suggests that particle formation would proceed through low-temperature nucleation involving clusters of a few PAH molecules held together by weak Van der Waals forces.

In the work of Wong *et al.* (2000), many kinetic rate coefficients had to be estimated and many possible ion-neutral reactions that may be important were ignored. As pointed out by Pryor and Hord (1991), most ion and ion-neutral reactions are faster than similar reactions involving radical species. These sorts of reactions may dominate the synthesis of complex hydrocarbons in the auroral zones. To examine their effect, A. Wong *et al.* (2003) developed an improved auroral chemical model with updated neutral and ion kinetics and, by analogy with Earth, more effective eddy mixing in the polar regions. Their ion chemistry included 288 charge exchange and 79 electron-ion recombination reactions selected from over 4000 reactions in the literature. Again, many rate coefficients had to be estimated. They found that ion chemistry accounted for more than 80% of the benzene production in their model and that the benzene column abundance that developed was similar to the mid-latitude value derived by Bézard *et al.* (2001). In addition, ion chemistry and more vigorous eddy mixing in the auroral regions was found to lead to significant enhancement of PAH production rates. This proves to be important for the pre-

diction of the total volume of polar haze that can be formed by the auroral chemistry, as discussed below.

Aerosol microphysical models for the stratospheric haze have been formulated by Moreno (1996), Banfield *et al.* (1998a), Friedson *et al.* (2002), and A. Wong *et al.* (2003). All the models are one-dimensional. Moreno calculated vertical profiles of haze particle size and concentration for equatorial and south polar latitudes. The computed profiles were then input into a radiative transfer code to produce simulated center-to-limb I/F profiles (where I is the reflected intensity and πF is the incident solar flux), which were subsequently compared to center-to-limb data constructed from a set of HST images acquired in the near-ultraviolet. Moreno did not attempt to model the nucleation process in detail. Instead, it was assumed that tiny primary particles of radius $\sim 0.01 \mu\text{m}$ are produced at high altitudes by chemical reactions between hydrocarbons. They were then allowed to subsequently grow by Brownian coagulation and hydrazine condensation, and undergo sedimentation and eddy diffusion. The particles were assumed to be spherical in shape and were allowed to possess a charge. At low latitudes, hydrazine condensation was found to dominate particle growth. For the model that provided a best fit to the center-to-limb data, mean particle radii were calculated to be less than $\sim 0.03 \mu\text{m}$ above the 100-mbar level. These radii are significantly smaller than the values of $\sim 0.2\text{--}0.5 \mu\text{m}$ estimated from the observations of Tomasko *et al.* (1986) and from analysis of *Galileo* SSI and HST images (Rages *et al.* 1999).

For the south polar region, Moreno estimated the mass production rate of haze to be ~ 1500 times greater than that near the equator as a result of auroral particle precipitation. For this reason, hydrazine condensation was found to be less important in the polar region. Electrically neutral particles attained a mean radius $\sim 0.2 \mu\text{m}$ near and below the 100-mbar level, decreasing in size to about $0.1 \mu\text{m}$ near the 20-mbar level. In Moreno's best-fit model, the particles were assumed to have a small charge. For this case, mean radii remained below $\sim 0.07 \mu\text{m}$ and the column optical depth at $0.255\text{-}\mu\text{m}$ wavelength was ~ 8 . The mean radii are somewhat smaller than values derived by Tomasko *et al.* (1986) for 40°N latitude and by Rages *et al.* (1999) for 60°N .

Friedson *et al.* (2002) coupled the neutral chemical kinetics results of Wong *et al.* (2000) with an aerosol microphysics code to propose a detailed model for the formation and growth of polar haze particles. Later the work was updated to include the ion chemistry model of A. Wong *et al.* (2003) and the implications for aerosol formation were reported in that paper. A schematic diagram of the basic physical processes included in these models is shown in Figure 5.14. The microphysics calculations included homogeneous and heterogeneous nucleation, Brownian coagulation between electrically neutral particles, condensation of condensible complex hydrocarbons (but not hydrazine), eddy diffusive transport, and particle sedimentation. Coagulation between particles was assumed to produce aggregates possessing a single, characteristic fractal dimension lying between 2 and 3. The fractal dimension was allowed to assume different values in different model runs in order to study the effect of particle shape on predicted mean radii and concentrations. Friedson *et al.* (2002) predicted that A_4 (pyrene, a PAH consisting of four fused rings) homogeneously nucleates at high altitudes to form tiny primary particles. At

lower altitudes, A_3 (phenanthrene) and A_2 (naphthalene) heterogeneously nucleate on the A_4 nuclei. The particles grow by coagulation and additional condensation of A_2 and A_3 on the nucleated particles and eventually sediment out to the troposphere. Predicted particle mean sizes and total aerosol loading varied somewhat according to the value adopted for the assumed fractal dimension of the aggregates, with the least-compact aggregations growing to the largest sizes. Aggregates of fractal dimension 2.5 developed mean volumes equal to a sphere of radius $\sim 0.5 \mu\text{m}$ near the 20-mbar pressure level. Irrespective of the dimension of the aggregates, mean particle volume decreases with increasing altitude, as expected for a system approximately in sedimentation-coagulation equilibrium. The range of altitudes where aerosol formation is predicted to occur and the predicted mean size of particles appear to be generally consistent with the observations. For the results based on neutral chemistry (Friedson *et al.* 2002), the total amount of aerosol loading predicted by the model fell up to two orders of magnitude short of that inferred by Tomasko *et al.* (1986) for 40°N planetocentric latitude. A. Wong *et al.* (2003) demonstrate that the inclusion of ion chemistry and larger polar eddy diffusion coefficient enhances PAH production significantly and produces a total volume of polar haze per unit area of $\sim 1 \times 10^{-5} \text{ cm}^3 \text{ cm}^{-2}$, which lies within the range allowed by the observations. However, they also remark that great uncertainties remain in our current understanding of polar haze production. Measurements of (i) the reaction kinetics of the ring production process at low temperatures, (ii) the energy spectrum and total energy flux of electrons in the jovian auroras, (iii) the chemical, physical and optical properties of the polar aerosols, and (iv) the magnitude of eddy diffusion at the auroral latitudes are all needed to make further progress.

5.5 SUMMARY

Recent observations by instruments on the *Galileo* probe, the orbiter, the Hubble Space Telescope, and ground-based telescopes have added a great deal to the many observations of Jupiter from earlier ground-based and space-based instruments. Our models are now sophisticated enough to account in a basic way for most of the observations. Figure 5.15 summarizes the current view of tropospheric cloud structure. Like Figure 5.6, this figure is intended to characterize the principal features of the jovian tropospheric cloud structure, including variations in cloud altitude. Except for hot spots and the Great Red Spot, structures for individual regions (like the thunderstorms and ovals) are not shown.

Before we summarize the main features of the tropospheric cloud structure depicted in Figure 5.15, we wish to reiterate that there remain multiple interpretations of some of the data. These different interpretations are inspired by different data sets which have different spatial resolutions and spectral coverage, or are unique in some other way. For example, small-scale reflectivity variations seen in the high spatial resolution ($\sim 30 \text{ km}$) *Galileo* SSI images figure prominently in the Banfield *et al.* (1998b) cloud models, and these features are not resolved in any other data set. Similarly unique are the dense spectral coverage of the NIMS data and the very specific in situ measurements by

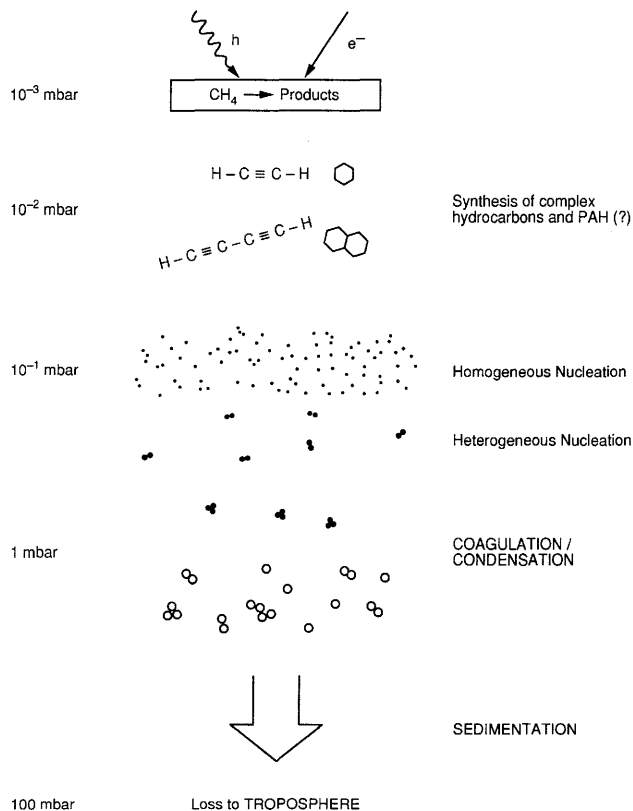


Figure 5.14. Schematic diagram of physical processes included in the coupled chemical-aerosol microphysical model of Friedson *et al.* (2002).

the *Galileo* probe Nephelometer and Net Flux Radiometer. At the same time, models of these data require that some assumptions be made about parameters which influence the observed quantities but are not very well constrained by them. The phase functions of the scattering particles and their dependence on altitude and latitude is one important example of this.

Perhaps most unsettling are the two treatments of the single scattering albedo of the particles and gas at continuum wavelengths in the near-infrared. West *et al.* (1986) and many others believed the continuum contrasts to be caused chiefly by variations in the single scattering albedo of the particles (produced by constituents such as those listed in Table 5.3). This is certainly the case at blue wavelengths. Banfield *et al.* (1998b) and Sromovsky and Fry (2002) prefer a model with the particles as conservative scatterers (at near-infrared wavelengths), but with the continuum contrasts produced by variations in optical depth. In order for that mechanism to work, some absorption, either from methane gas, H_2 or some other trace gas or particles, must be distributed more or less uniformly with the H_2 or concentrated beneath the water cloud. In the absence of this hypothetical absorber, conservative Rayleigh scattering from the underlying optically thick gas will produce a highly reflective atmosphere. If from methane or H_2 , this absorber must be more strongly absorbing than we can understand from current theory or laboratory measurements or from the absorption coefficients derived by Karkoschka (1998).

Both approaches to the continuum question have merit

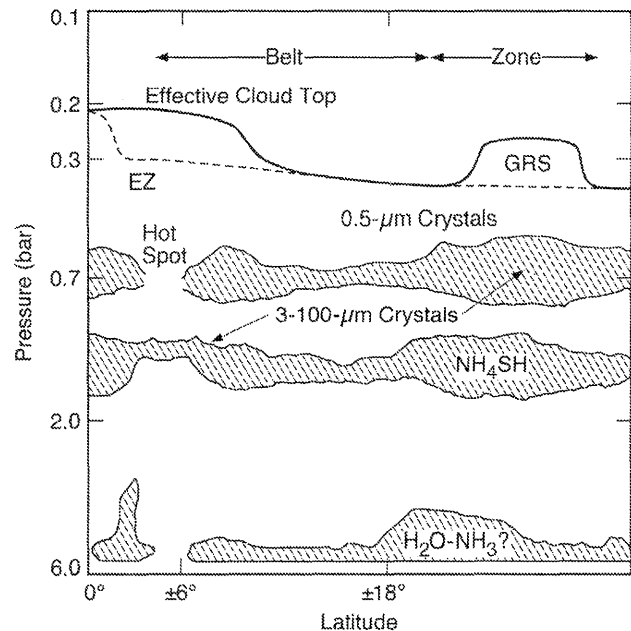


Figure 5.15. This schematic represents ideas about tropospheric cloud structure synthesized from a large collection of observations. The upper haze populated by sub-micron particles is shown to extend between the top of a denser, larger-particle cloud around 500 mbar to as high as 200 mbar near the equator and over the GRS. The elevated haze near the equator is actually not symmetric about the equator but resides in the latitude band 0° to 9° N. This is indicated by the solid and dashed curves that apply to the northern and southern latitudes, respectively. The elevated haze above the GRS is also shown as a solid curve, while other longitudes follow the dashed curve. A variation to this view favored by Sromovsky and Fry (2002) calls for an optically and physically thinner upper tropospheric haze confined to the highest altitudes but still below the cloud top boundary shown here. Chromophores are present in the upper haze and may be present also in deeper layers. The small-scale contrasts seen in *Galileo* SSI images point to cloud variations near 750 ± 200 mbar. Radiative transfer models of variations in the *Galileo* NIMS near-infrared spectra favor cloud variations at deeper levels, centered near the 1.5 bar pressure level. Observations probing the deeper water/ammonia cloud region are sparse. The *Galileo* probe found no water cloud in the hot spot it descended through. There are small regions often associated with lightning where the upper haze and cloud are more transparent and deeper clouds are seen alongside small regions of higher, thicker clouds (see the section on *Galileo* SSI results).

and at present we cannot rule out either, but they have very different consequences for cloud models. We look to future investigations to do a better job of differentiating between these possibilities and of tying together and synthesizing the large and growing collection of data from many sources. All of the key observations need to be brought under the umbrella of a single model. A more thorough analysis of the wavelength dependence of limb darkening from HST and *Cassini* imaging data may help, combined with analyses of the phase angle behavior of the reflectivity from UV to near-IR wavelengths from *Galileo* and *Cassini* observations. For now we attempt to summarize as best we can in the following paragraphs a model which accounts for the aggregated body of evidence we have presented.

Contrasts at $45 \mu\text{m}$ (Gierasch *et al.* 1986) and at spatial

scales ~ 30 km seen in *Galileo* SSI images (Banfield *et al.* 1998b) are reproduced in models having a nearly-uniform high haze of sub-micron particles overlying a physically thin cloud of larger particles in the pressure range 0.9–0.5 bars whose optical depth varies considerably from place to place. The upper tropospheric haze is highest and thickest over the North Equatorial Belt and the Great Red Spot where it reaches pressure levels near 200 mbar. It is nearly transparent to upwelling $5 \mu\text{m}$ thermal radiation. Evidence for a deeper cloud comes from near-infrared spectra at lower spatial resolution. The analysis of NIMS data by Irwin and Dyudina (2002) put the deeper cloud in the pressure range 1–2 bar. A recent re-assessment of methane absorption coefficients (Irwin, private communication 2002) puts the centroid of this cloud at 1.5 bars. This cloud is probably ammonium hydrosulfide but water ice is also a candidate. Optical depth in this cloud and in the higher thin cloud sensed in SSI images together account for the strong spatial variations in the $5 \mu\text{m}$ images.

There is almost no observational evidence for a deep water cloud except for a few small regions. It is difficult or impossible to sense the deep water cloud in places where the overlying clouds are optically thick (mostly in zones). Interestingly, those regions that appear to show a deep water cloud (deeper than the 3 bar pressure level) are usually close to a region of high, thick clouds, according to Banfield *et al.* (1998b).

There is some controversy about the optical thickness of the high tropospheric haze. It can be as low as about 2 at visible wavelengths if the haze is confined to a region near its upper boundary (200–400 mbar). This model is consistent with the *Galileo* probe Net Flux Radiometer measurements. Sromovsky and Fry (2002) show that it also provides a good fit to a variety of bright and dark features in the North Equatorial Belt. This model may be appropriate for an even larger range of latitudes. If so, Figure 5.15 should be modified to show a gap in particle density between about 300 and 500 mbar (and an even larger gap in hot spots). Other studies favor higher optical depths (up to 8) distributed over a larger vertical extent over most of Jupiter. Ambiguity in the interpretation of reflected sunlight makes this distinction difficult, but certainly the probe NFR results favor the smaller optical depth.

Most retrievals of particle size derive mean radii $\sim 0.5 \mu\text{m}$ in the upper tropospheric haze. This is a little smaller than the number indicated in Figure 5.6. Deeper in the atmosphere, both remote sensing and in situ measurements from the *Galileo* probe Nephelometer indicate larger particles, with a mean radius of several microns. In isolated locations where ammonia ice spectra are observed the particle mean radius is probably near $10 \mu\text{m}$.

If the particle composition of the upper few optical depths is ammonia we would expect to see strong ammonia absorption features near $3 \mu\text{m}$ and near 9.4 and $26 \mu\text{m}$. The ISO spectra have been interpreted as showing evidence for mostly larger ($10 \mu\text{m}$) ammonia ice particles. Those observations averaged a large region of Jupiter. It is not known if the small-scale ammonia ice features reported by Baines *et al.* (2002) can be reconciled with the interpretation of ISO spectra by Brooke *et al.* (1998). A narrow feature at $9.4 \mu\text{m}$ has been detected in *Cassini* CIRS spectra (M.H. Wong *et al.* 2004) but only in restricted latitude bands, and the

spatial morphology of this feature differs from that seen in the NIMS data. This difference is understandable if the $9.4 \mu\text{m}$ feature senses the higher sub-micron particles while the NIMS data senses larger particles associated with specific meteorological features. One of the outstanding questions is why ammonia ice features are confined to a few percent of the area. Perhaps a coating of hydrazine ice is able to block ammonia ice spectral features. More laboratory work on the spectral behavior of hydrazine ice in the infrared and also in the ultraviolet would help answer this question. The composition of chromophores is also not resolved. Recent work with empirical orthogonal functions (Simon-Miller *et al.* 2001a) strengthens the idea that very few colored constituents (two or three) are needed to account for the variations in color, and that coating by or mixing with ammonia ice in zones as well as in belts accounts for most of the albedo variation at blue wavelengths.

The collection of observations coupled with modeling results and theory have advanced our understanding of jovian clouds and haze to a remarkable degree during the past three decades. Much remains to be done, however. Among the most persistent questions is the composition of the chromophores. Another big question is the composition of most of the bright white particles. Spectral signatures for ammonia ice are expected but not seen except in local regions over a very small fraction of the area. We also do not know to what extent vertical motions carry condensibles like water and ammonium hydrosulfide to higher levels. The uppermost cloud visible to us may be a mixture of all three. Water ice signatures have been observed in *Voyager* IRIS spectra but only over about 1% of the planet (Simon-Miller *et al.* 2000). New measurements sensitive to the deep water cloud are needed to reveal its presence in regions not accessible to current remote sensing techniques. More could be done with present data to reveal cloud structures for small-scale features and to tie these to ideas about dynamical processes.

Some of the newest and most exciting results to come from Jupiter studies pertain to the polar stratospheric haze. At low latitudes the stratospheric haze is optically thin (estimates ranging from 0.05 to 0.3 at visible and near-IR wavelengths) and nearly uniformly distributed in latitude. At high latitudes the haze morphology is richly textured. Features seen in the near-UV and in the strong methane bands are probably near the 1–3 mbar pressure level. A multitude of wave features equatorward of 60° planetocentric latitude are seen in the stratosphere but are not apparent at wavelengths which sense the troposphere. Poleward of latitude 60° we have seen the formation of a large dark oval on two occasions as well as a number of smaller features. A connection with Jupiter's aurora is apparent from the distribution of the haze, but the details which connect auroral processes with haze formation are not well understood. Recent progress on hydrocarbon chemistry and microphysics is advancing our understanding of those issues. Much remains to be done to comprehend the highly coupled auroral/chemical/dynamical and microphysical nature of the stratospheric haze and what it can tell us about polar processes.

The outstanding questions on the topics of tropospheric and stratospheric clouds and hazes are:

- Why are the spectral signatures of ammonia ice confined to a small fraction of the planet when it appears that

a sub-micron upper tropospheric haze is ubiquitous? Why has the feature at 26 μm not been observed?

- What produces contrast at red and near-infrared continuum wavelengths?

- Is the chromophore mixed in the ammonia and ammonium hydrosulfide ice clouds (in the blue this is certainly the case), or are chromophores mixed uniformly to deep levels with the gas or concentrated at deeper levels, or possibly far-wing pressure-induced H_2 or methane gas opacity that has previously been underestimated? A semi-infinite Rayleigh-scattering gas with white ammonia or ammonium hydrosulfide or water clouds is white. The answer to this question has broader implication for cloud optical depths derived using weak methane and continuum wavelengths.

- What produces the colors of the clouds?

- How do we account for the formation and evolution of the large (25 000 km) dark high-latitude oval seen twice since 1994 and only in UV images?

Acknowledgements. We benefited from careful reviews by L. Sromovsky and two anonymous referees. Part of this work was performed by the Jet Propulsion Laboratory, California Institute of Technology.

REFERENCES

- Ackerman, A. S. and M. S. Marley, Precipitating condensation clouds in substellar atmospheres, *ApJ* **556**, 872–884, 2001.
- Allison, M., Planetary waves in Jupiter's equatorial atmosphere, *Icarus* **83**, 282–307, 1990.
- Atkinson, D. H., J. B. Pollack, and A. Seiff, The *Galileo* probe doppler wind experiment: Measurement of the deep zonal winds on Jupiter, *J. Geophys. Res.* **103**, 22 911–22 928, 1998.
- Atreya, S. K., M. H. Wong, T. C. Owen, H. B. Niemann, and P. R. Mahaffy, Chemistry and clouds of Jupiter's atmosphere: A *Galileo* perspective, in *The Three Galileos: the Man, the Spacecraft, the Telescope*, p. 249, 1997.
- Atreya, S. K., M. H. Wong, T. C. Owen, P. R. Mahaffy, H. B. Niemann, I. de Pater, P. Drossart, and T. Encrenaz, A comparison of the atmospheres of Jupiter and Saturn: Deep atmospheric composition, cloud structure, vertical mixing, and origin, *Planet. Space Sci.* **47**, 1243–1262, 1999.
- Axel, L., Inhomogeneous models of the atmosphere of Jupiter, *ApJ* **173**, 451, 1972.
- Baines, K. H. and J. T. Bergstralh, The structure of the Uranian atmosphere: Constraints from the geometric albedo spectrum and H_2 and CH_4 line profiles, *Icarus* **65**, 406–441, 1986.
- Baines, K. H., R. A. West, L. P. Giver, and F. Moreno, Quasi-random narrow-band model fits to near-infrared low-temperature laboratory methane spectra and derived exponential-sum absorption coefficients, *J. Geophys. Res.* **98**, 5517–5529, 1993.
- Baines, K. H., R. W. Carlson, and L. W. Kamp, Fresh ammonia ice clouds in Jupiter: I. Spectroscopic identification, spatial distribution, and dynamical implications, *Icarus* **159**, 74–94, 2002.
- Banfield, D., B. J. Conrath, P. J. Gierasch, P. D. Nicholson, and K. Matthews, Near-IR spectrophotometry of jovian aerosols: Meridional and vertical distributions, *Icarus* **134**, 11–23, 1998a.
- Banfield, D., P. J. Gierasch, M. Bell, E. Ustinov, A. P. Ingersoll, A. R. Vasavada, R. A. West, and M. J. S. Belton, Jupiter's cloud structure from *Galileo* imaging data, *Icarus* **135**, 230–250, 1998b.
- Beebe, R. F. and T. A. Hockey, A comparison of red spots in the atmosphere of Jupiter, *Icarus* **67**, 96–105, 1986.
- Beebe, R. F., G. S. Orton, and R. A. West, Time-variable nature of the jovian cloud properties and thermal structure: An observational perspective, in *Time-Variable Phenomena in the Jovian System*, M. J. S. Belton, R. A. West, J. Rahe (eds), NASA-SP-494, pp. 245–288, 1989.
- Bézar, B., P. Drossart, T. Encrenaz, and H. Feuchtgruber, Benzene on the giant planets, *Icarus* **154**, 492–500, 2001.
- Birnbaum, G. and E. R. Cohen, Theory of line shape in pressure-induced absorption, *J. Can. Phys.* **54**, 593–602, 1976.
- Borysow, A., Modeling of collision-induced infrared absorption spectra of H_2 – H_2 pairs in the fundamental band at temperatures from 20 to 300 K, *Icarus* **92**, 273–279, 1991.
- Borysow, A., New model of collision-induced infrared absorption spectra of H_2 –He pairs in the 2–2.5 micron range at temperatures from 20 to 300 K: An update, *Icarus* **96**, 169–175, 1992.
- Borysow, J., L. Frommhold, and G. Birnbaum, Collision-induced rototranslational absorption spectra of H_2 –He pairs at temperatures from 40 to 3000 K, *ApJ* **326**, 509–515, 1988.
- Braak, C. J., J. F. de Haan, J. W. Hovenier, and L. D. Travis, *Galileo* photopolarimetry of Jupiter at 678.5 nm, *Icarus* **157**, 401–418, 2002.
- Brooke, T. Y., R. F. Knacke, T. Encrenaz, P. Drossart, D. Crisp, and H. Feuchtgruber, Models of the ISO 3- μm reflection spectrum of Jupiter, *Icarus* **136**, 1–13, 1998.
- Brown, L. R. and J. S. Margolis, Empirical line parameters of NH_3 from 4791–5294 cm^{-1} , *J. Quant. Spectrosc. Radiat. Trans.* **56**, 283–294, 1996.
- Cameron-Smith, P. J., Ph.D. thesis, University of Oxford, 1998.
- Carlson, B. E., W. B. Rossow, and G. S. Orton, Cloud microphysics of the giant planets, *J. Atmos. Sci.* **45**, 2066–2081, 1988.
- Carlson, R. W., P. R. Weissman, W. D. Smythe, and J. C. Mahoney, Near-Infrared Mapping Spectrometer experiment on *Galileo*, *Space Sci. Rev.* **60**, 457–502, 1992.
- Chan, Y. M. and A. Dalgarno, The refractive index of helium, *Proc. Phys. Soc.* **85**, 227–230, 1965.
- Chanover, N. J., D. M. Kuehn, and R. F. Beebe, Vertical structure of Jupiter's atmosphere at the *Galileo* probe entry latitude, *Icarus* **128**, 294–305, 1997.
- Clarke, J. T., J. Ajello, G. Ballester, L. Ben Jaffel, J. Connerney, J.-C. Gérard, G. R. Gladstone, D. Grodent, W. Pryor, J. Trauger, and J. H. Waite, Ultraviolet emissions from the magnetic footprints of Io, Ganymede and Europa on Jupiter, *Nature* **415**, 997–1000, 2002.
- Cowley, S. W. H. and E. J. Bunce, Origin of the main auroral oval in Jupiter's coupled magnetosphere-ionosphere system, *Planet. Space Sci.* **49**, 1067–1088, 2001.
- DeWoody, B. A., W. R. Pryor, E. S. Barker, R. A. West, C. Y. Na, W. E. Colwell, and W. K. Tobiska, Imaging and spectroscopy of Jupiter from McDonald Observatory and *Galileo*, *AAS/DPS* **33**, 0, 2001.
- Doose, L. R., M. G. Tomasko, and N. D. Castillo, The single scattering phase functions of Jupiter's clouds, in *Proceedings of the Conference on the Jovian Atmospheres*, NASA CP-2441, M. Allison and L. D. Travis (Eds.), pp. 83–93, 1986.
- Drossart, P., M. Roos-Serote, T. Encrenaz, E. Lellouch, K. H. Baines, R. W. Carlson, L. W. Kamp, G. S. Orton, S. Calcutt, P. Irwin, F. W. Taylor, and A. Weir, The solar reflected component in Jupiter's 5-micron spectra from NIMS/*Galileo* observations, *J. Geophys. Res.* **103**, 23 043–23 050, 1998.
- Fink, U. and G. T. Sill, The infrared spectral properties of frozen volatiles, in *Comets*, L. L. Wilkening (ed), University of Arizona Press, pp. 164–202, 1982.
- Fink, U., D. C. Benner, and K. A. Dick, Band model analysis of laboratory methane absorption spectra from 4500 to 10 500 \AA , *J. Quant. Spectrosc. Radiat. Trans.* **18**, 447–457, 1977.

- Ford, A. L. and J. C. Browne, Rayleigh and Raman cross sections for the hydrogen molecule, *Atomic Data* **5**, 305–313, 1973.
- Friedson, A. J., Water, ammonia and H₂S mixing ratios in Jupiter's five-micron hot spots: A dynamical model, *Icarus* **submitted**, 2003.
- Friedson, A. J., A. Wong, and Y. L. Yung, Models for polar haze formation in Jupiter's stratosphere, *Icarus* **158**, 389–400, 2002.
- Gierasch, P. J., J. A. Magalhaes, and B. J. Conrath, Zonal mean properties of Jupiter's upper troposphere from *Voyager* infrared observations, *Icarus* **67**, 456–483, 1986.
- Gierasch, P. J., A. P. Ingersoll, D. Banfield, S. P. Ewald, P. Helfenstein, A. Simon-Miller, A. Vasavada, H. H. Breneman, D. A. Senske, and the *Galileo* Imaging Team, Observation of moist convection in Jupiter's atmosphere, *Nature* **403**, 628–630, 2000.
- Giver, L. P., Intensity measurements of the CH₄ bands in the region 4350 Å to 10600 Å, *J. Quant. Spectrosc. Radiat. Trans.* **19**, 311–322, 1978.
- Gladstone, G. R., J. H. Waite, D. Grodent, W. S. Lewis, F. J. Cray, R. F. Elsner, M. C. Weisskopf, T. Majeed, J.-M. Jahn, A. Bhardwaj, J. T. Clarke, D. T. Young, M. K. Dougherty, S. A. Espinosa, and T. E. Cravens, A pulsating auroral X-ray hot spot on Jupiter, *Nature* **415**, 1000–1003, 2002.
- Goody, R., R. West, L. Chen, and D. Crisp, The correlated-*k* method for radiation calculations in nonhomogeneous atmospheres, *J. Quant. Spectrosc. Radiat. Trans.* **43**, 191–199, 1989.
- Goody, R. M. and Y. L. Yung, *Atmospheric Radiation: Theoretical Basis*, Oxford University Press, 1989.
- Gradie, J. and J. Veverka, Photometric properties of powdered sulfur, *Icarus* **58**, 227–245, 1984.
- Guelachvili, G. A., A. Abdulah, N. Tu, K. Narahari Rao, S. Urban, and D. Papoušek, High-resolution Fourier transform spectra of ¹⁴NH₃ at 3.0 μm, *J. Mol. Spectrosc.* **133**, 345–364, 1989.
- Gurnett, D. A., W. S. Kurth, G. B. Hospodarsky, A. M. Persoon, P. Zarka, A. Lecacheux, S. J. Bolton, M. D. Desch, W. M. Farrell, M. L. Kaiser, H.-P. Ladreiter, H. O. Rucker, P. Galopeau, P. Louarn, D. T. Young, W. R. Pryor, and M. K. Dougherty, Control of Jupiter's radio emission and aurorae by the solar wind, *Nature* **415**, 985–987, 2002.
- Hord, C. W., R. A. West, K. E. Simmons, D. L. Coffeen, M. Sato, A. L. Lane, and J. T. Bergstralh, Photometric observations of Jupiter at 2400 angstroms, *Science* **206**, 956–959, 1979.
- Howland, G. R., P. Harteck, and R. R. Reeves, The role of phosphorus in the upper atmosphere of Jupiter, *Icarus* **37**, 301–306, 1979.
- Hueso, R. and A. Sánchez-Lavega, A three-dimensional model of moist convection for the giant planets: The Jupiter case, *Icarus* **151**, 257–274, 2001.
- Huffman, D. R. and C. F. Bohren, Infrared absorption spectra of nonspherical particles treated in the Rayleigh-ellipsoid approximation, in *Light Scattering by Irregularly Shaped Particles*, D. Schuerman, ed., pp. 103–111, Plenum, 1980.
- Huntress, W. T. and V. G. Anicich, Colored sulfur species in the atmosphere of Jupiter, *BAAS* **16**, 648, 1984.
- Huntress, W. T. and L. Thorne, Colored sulfur ions in the atmosphere of Jupiter, *BAAS* **14**, 723, 1982.
- Ingersoll, A. P., P. J. Gierasch, D. Banfield, A. R. Vasavada, and the *Galileo* Imaging Team, Moist convection as an energy source for the large-scale motions in Jupiter's atmosphere, *Nature* **403**, 630–632, 2000.
- Irwin, P. G. J. and U. Dyudina, The retrieval of cloud structure maps in the equatorial region of Jupiter using a principal component analysis of *Galileo*/NIMS data, *Icarus* **156**, 52–63, 2002.
- Irwin, P. G. J., S. B. Calcutt, F. W. Taylor, and A. L. Weir, Calculated *k* distribution coefficients for hydrogen- and self-broadened methane in the range 2000–9500 cm⁻¹ from exponential sum fitting to band-modelled spectra, *J. Geophys. Res.* **101**, 26137–26154, 1996.
- Irwin, P. G. J., S. B. Calcutt, K. Sihra, F. W. Taylor, A. L. Weir, J. Ballard, and W. B. Johnston, Band parameters and coefficients for self-broadened ammonia in the range 4000 to 11000 cm⁻¹, *J. Quant. Spect. Rad. Transf.* **62**, 193–204, 1998a.
- Irwin, P. G. J., A. L. Weir, S. E. Smith, F. W. Taylor, A. L. Lambert, S. B. Calcutt, P. J. Cameron-Smith, R. W. Carlson, K. Baines, G. S. Orton, P. Drossart, T. Encrenaz, and M. Roos-Serote, Cloud structure and atmospheric composition of Jupiter retrieved from *Galileo* Near-Infrared Mapping Spectrometer real-time spectra, *J. Geophys. Res.* **103**, 23001–23022, 1998b.
- Irwin, P. G. J., A. L. Weir, F. W. Taylor, S. B. Calcutt, and R. W. Carlson, The origin of belt/zone contrasts in the atmosphere of Jupiter and their correlation with 5-μm opacity, *Icarus* **149**, 397–415, 2001.
- Karkoschka, E., Methane, ammonia, and temperature measurements of the jovian planets and Titan from CCD-spectrophotometry, *Icarus* **133**, 134–146, 1998.
- Kaye, J. A. and D. F. Strobel, HCN formation on Jupiter: The coupled photochemistry of ammonia and acetylene, *Icarus* **54**, 417–433, 1983.
- Khare, B. N. and C. Sagan, Red clouds in reducing atmospheres, *Icarus* **20**, 311, 1973.
- Khare, B. N. and C. Sagan, Cyclic octatomic sulfur: A possible infrared and visible chromophore in the clouds of Jupiter, *Science* **189**, 722, 1975.
- Khare, B. N., C. Sagan, E. T. Arakawa, F. Suits, T. A. Callcott, and M. W. Williams, Optical constants of organic tholins produced in a simulated Titanian atmosphere: From soft X-ray to microwave frequencies, *Icarus* **60**, 127–137, 1984.
- Kim, S. J., J. Caldwell, A. R. Rivolo, R. Wagener, and G. S. Orton, Infrared polar brightening on Jupiter: III. Spectrometry from the *Voyager 1* IRIS experiment, *Icarus* **64**, 233–248, 1985.
- Kuehn, D. M. and R. F. Beebe, A study of the time variability of Jupiter's atmospheric structure, *Icarus* **101**, 282–292, 1993.
- Larson, H. P., G. L. Bjoraker, D. S. Davis, and R. Hofmann, The jovian atmospheric window at 2.7 microns: A search for H₂S, *Icarus* **60**, 621–639, 1984.
- Lewis, J. S., The clouds of Jupiter and the NH₃-H₂O and NH₃-H₂S systems, *Icarus* **10**, 365–378, 1969.
- Lewis, J. S. and M. B. Fegley, Vertical distribution of disequilibrium species in Jupiter's troposphere, *Space Sci. Rev.* **39**, 163–192, 1984.
- Lewis, J. S. and R. G. Prinn, Jupiter's clouds: Structure and composition, *Science* **169**, 472–473, 1970.
- Limaye, S. S., Jupiter: New estimates of the mean zonal flow at the cloud level, *Icarus* **65**, 335–352, 1986.
- Lunine, J. I., W. B. Hubbard, A. Burrows, Y.-P. Wang, and K. Garlow, The effect of gas and grain opacity on the cooling of brown dwarfs, *ApJ* **338**, 314–337, 1989.
- Marley, M. S., C. Gelino, D. Stephens, J. I. Lunine, and R. Freedman, Reflected spectra and albedos of extrasolar giant planets: I. Clear and cloudy atmospheres, *ApJ* **513**, 879–893, 1999.
- Mauk, B. H., J. T. Clarke, D. Grodent, J. H. Waite, C. P. Paranicas, and D. J. Williams, Transient aurora on Jupiter from injections of magnetospheric electrons, *Nature* **415**, 1003–1005, 2002.
- McKellar, A. R. W. and H. L. Welsh, Collision-induced spectra of hydrogen in the first and second overtone regions with applications to planetary atmospheres, *Proc. R. Soc. London Ser. A.* **322**, 421–434, 1971.
- Minton, R. B., Latitude measures of Jupiter in the 0.89 μm

- methane band, *Comm. Lunar Planet. Lab.* **9**, 339–351, 1972.
- Moreno, F., The structure of the stratospheric aerosol layer in the equatorial and south polar regions of Jupiter, *Icarus* **124**, 632–644, 1996.
- Niemann, H. B., S. K. Atreya, G. R. Carignan, T. M. Donahue, J. A. Haberman, D. N. Harpold, R. E. Hartle, D. M. Hunten, W. T. Kasprzak, P. R. Mahaffy, T. C. Owen, N. W. Spencer, and S. H. Way, The *Galileo* probe mass spectrometer: Composition of Jupiter's atmosphere, *Science* **272**, 846–849, 1996.
- Niemann, H. B., S. K. Atreya, G. R. Carignan, T. M. Donahue, J. A. Haberman, D. N. Harpold, R. E. Hartle, D. M. Hunten, W. T. Kasprzak, P. R. Mahaffy, T. C. Owen, and S. H. Way, The composition of the jovian atmosphere as determined by the *Galileo* probe mass spectrometer, *J. Geophys. Res.* **103**, 22 831–22 846, 1998.
- Noy, N., A. Bar-Nun, and M. Podolak, Acetylene photopolymers in Jupiter's stratosphere, *Icarus* **40**, 199–204, 1979.
- Noy, N., M. Podolak, and A. Bar-Nun, Photochemistry of phosphine and Jupiter's Great Red Spot, *J. Geophys. Res.* **86**, 11 985–11 988, 1981.
- O'Brien, J. J. and H. Cao, Absorption spectra and absorption coefficients for methane in the 750–940 nm region obtained by intracavity laser spectroscopy, *J. Quant. Spectrosc. Radiat. Trans.* **75**, 323–350, 2002.
- Ortiz, J. L., G. S. Orton, A. J. Friedson, S. T. Stewart, B. M. Fisher, and J. R. Spencer, Evolution and persistence of 5-micron hot spots at the *Galileo* probe entry latitude, *J. Geophys. Res.* **103**, 23 051–23 070, 1998.
- Orton, G. S., B. M. Fisher, K. H. Baines, S. T. Stewart, A. J. Friedson, J. L. Ortiz, M. Marinova, M. Ressler, A. Dayal, W. Hoffmann, J. Hora, S. Hinkley, V. Krishnan, M. Masanovic, J. Tesic, A. Tziolas, and K. C. Parija, Characteristics of the *Galileo* probe entry site from Earth-based remote sensing observations, *J. Geophys. Res.* **103**, 22 791–22 814, 1998.
- Owen, T. and H. P. Mason, New studies of Jupiter's atmosphere, *J. Atmos. Sci.* **26**, 870–873, 1969.
- Owen, T. and R. J. Terrile, Colors on Jupiter, *J. Geophys. Res.* **86**, 8797–8814, 1981.
- Ponnamperuma, C., The organic chemistry and biology of the atmosphere of the planet Jupiter, *Icarus* **29**, 321, 1976.
- Ponnamperuma, C. and P. Molton, The prospect of life on Jupiter, *Space Life Sci.* **4**, 32–44, 1973.
- Pope, S. K., M. G. Tomasko, M. S. Williams, M. L. Perry, L. R. Doose, and P. H. Smith, Clouds of ammonia ice: Laboratory measurements of the single-scattering properties, *Icarus* **100**, 203–220, 1992.
- Porco, C. C., R. A. West, A. McEwen, A. D. Del Genio, A. P. Ingersoll, P. Thomas, S. Squyres, L. Dones, C. D. Murray, T. V. Johnson, J. A. Burns, A. Brahic, G. Neukum, J. Veverka, J. M. Barbara, T. Denk, M. Evans, J. J. Ferrier, P. Geissler, P. Helfenstein, T. Roatsch, H. Throop, M. Tiscareno, and A. R. Vasavada, *Cassini* imaging of Jupiter's atmosphere, satellites, and rings, *Science* **299**, 1541–1547, 2003.
- Prinn, R. G. and J. S. Lewis, Phosphine on Jupiter and implications for the Great Red Spot, *Science* **190**, 274–276, 1975.
- Prinn, R. G. and T. Owen, Chemistry and spectroscopy of the jovian atmosphere, in *Jupiter*, T. Gehrels (ed), University of Arizona Press, pp. 319–371, 1976.
- Pryor, W. R. and C. W. Hord, A study of photopolarimeter system UV absorption data on Jupiter, Saturn, Uranus, and Neptune: Implications for auroral haze formation, *Icarus* **91**, 161–172, 1991.
- Ragent, B., D. S. Colburn, K. A. Rages, T. C. D. Knight, P. Avrin, G. S. Orton, P. A. Yanamandra-Fisher, and G. W. Grams, The clouds of Jupiter: Results of the *Galileo* Jupiter mission probe nephelometer experiment, *J. Geophys. Res.* **103**, 22 891–22 910, 1998.
- Rages, K., R. Beebe, and D. Senske, Jovian stratospheric hazes: The high phase angle view from *Galileo*, *Icarus* **139**, 211–226, 1999.
- Rice, F. O., Colors on Jupiter, *J. Chem. Phys.* **24**, 1259, 1956a.
- Rice, F. O., The chemistry of Jupiter, *Sci. Amer.* **194**, 6, 119–128, 1956b.
- Richter, H. and J. B. Howard, Formation of polycyclic aromatic hydrocarbons and their growth to soot: A review of chemical reaction pathways, *Progress in Energy and Combustion Science* **26**, 565–608, 2000.
- Roos-Serote, M., P. Drossart, T. Encrenaz, E. Lellouch, R. W. Carlson, K. H. Baines, L. Kamp, R. Mehlman, G. S. Orton, S. Calcutt, P. Irwin, F. Taylor, and A. Weir, Analysis of Jupiter North Equatorial Belt hot spots in the 4–5-micron range from *Galileo*/Near-Infrared Mapping Spectrometer observations: Measurements of cloud opacity, water, and ammonia, *J. Geophys. Res.* **103**, 23 023–23 042, 1998.
- Roos-Serote, M., A. R. Vasavada, L. Kamp, P. Drossart, P. Irwin, C. Nixon, and R. W. Carlson, Proximate humid and dry regions in Jupiter's atmosphere indicate complex local meteorology, *Nature* **405**, 158–160, 2000.
- Rosow, W. B., Cloud microphysics: Analysis of the clouds of Earth, Venus, Mars, and Jupiter, *Icarus* **36**, 1–50, 1978.
- Sagan, C. and B. N. Khare, Experimental jovian photochemistry: Initial Results, *ApJ* **168**, 563, 1971.
- Sagan, C. and S. L. Miller, Molecular synthesis in simulated reducing planetary atmospheres, *AJ* **65**, 499, 1960.
- Sagan, C. and E. E. Salpeter, Particles, environments, and possible ecologies in the jovian atmosphere, *ApJS* **32**, 737–755, 1976.
- Sanchez-Lavega, A., J. M. Gomez, J. Lecacheux, F. Colas, I. Miyazaki, D. Parker, and J. Guarro, The South Equatorial Belt of Jupiter: II. The onset and development of the 1993 disturbance, *Icarus* **121**, 18–29, 1996.
- Sanchez-Lavega, A., R. Hueso, and J. R. Acarreta, A system of circumpolar waves in Jupiter's stratosphere, *Geophys. Res. Lett.* **25**, 4043, 1998.
- Sasson, R., R. Wright, E. T. Arakawa, B. N. Khare, and C. Sagan, Optical properties of solid and liquid sulfur at visible and infrared wavelengths, *Icarus* **64**, 368–374, 1985.
- Scattergood, T. and T. Owen, On the sources of ultraviolet absorption in spectra of Titan and the outer planets, *Icarus* **30**, 780–788, 1977.
- Showman, A. P. and T. E. Dowling, Nonlinear simulations of Jupiter's 5-micron hot spots, *Science* **289**, 1737–1740, 2000.
- Showman, A. P. and A. P. Ingersoll, Interpretation of *Galileo* probe data and implications for Jupiter's dry downdrafts, *Icarus* **132**, 205–220, 1998.
- Sill, G., Reflection spectra of solids of planetary interest, *Comm. Lunar and Planet. Lab.* **10**, 1–7, 1973.
- Sill, G., U. Fink, and J. R. Ferraro, Absorption coefficients of solid NH₃ from 50 to 7000 cm⁻¹λ², *Opt. Soc. America* **70**, 724–739, 1980.
- Sill, G. T., The chemistry of the jovian cloud colors, in *Jupiter*, T. Gehrels (ed), University of Arizona Press, pp. 372–383, 1976.
- Simon-Miller, A. A., B. Conrath, P. J. Gierasch, and R. F. Beebe, A detection of water ice on Jupiter with *Voyager* IRIS, *Icarus* **145**, 454–461, 2000.
- Simon-Miller, A. A., D. Banfield, and P. J. Gierasch, An HST study of jovian chromophores, *Icarus* **149**, 94–106, 2001a.
- Simon-Miller, A. A., D. Banfield, and P. J. Gierasch, Color and the vertical structure in Jupiter's belts, zones, and weather systems, *Icarus* **154**, 459–474, 2001b.
- Singh, K. and J. J. O'Brien, Laboratory measurements of absorption coefficients for the 727-nm band of methane at 77 K and comparison with results derived from spectra of the giant planets, *J. Quant. Spectrosc. Radiat. Trans.* **54**, 607–619, 1995.

- Singh, K. and J. J. O'Brien, Absorption coefficients for the 727 nm band of methane at 77 K determined by intracavity laser spectroscopy, *Astrophys & Space Sci.* **236**, 97–109, 1996.
- Smith, D. W., Galilean satellite eclipse studies: II. Jovian stratospheric and tropospheric aerosol content, *Icarus* **44**, 116–133, 1980.
- Smith, P. H., The vertical structure of the jovian atmosphere, *Icarus* **65**, 264–279, 1986.
- Smith, P. H. and M. G. Tomasko, Photometry and polarimetry of Jupiter at large phase angles: II. Polarimetry of the South Tropical Zone, South Equatorial Belt, and the polar regions from the *Pioneer 10* and *11* missions, *Icarus* **58**, 35–73, 1984.
- Smith, W. H., C. P. Conner, and K. H. Baines, Absorption coefficients for the 6190 Å CH₄ band between 290 and 100 K with application to Uranus' atmosphere, *Icarus* **85**, 58–64, 1990.
- Sromovsky, L. A. and P. M. Fry, Jupiter's cloud structure as constrained by *Galileo* probe and HST observations, *Icarus* **157**, 373–400, 2002.
- Sromovsky, L. A., A. D. Collard, P. M. Fry, G. S. Orton, M. T. Lemmon, M. G. Tomasko, and R. S. Freedman, *Galileo* probe measurements of thermal and solar radiation fluxes in the jovian atmosphere, *J. Geophys. Res.* **103**, 22929–22978, 1998.
- Stam, D. M., D. Banfield, P. J. Gierasch, P. D. Nicholson, and K. Matthews, Near-IR spectrophotometry of saturnian aerosols: Meridional and vertical distribution, *Icarus* **152**, 407–422, 2001.
- Strobel, D. F., The photochemistry of NH₃ in the jovian atmosphere, *J. Atmos. Sci.* **30**, 1205–1209, 1973.
- Strobel, D. F., Photochemistry of the reducing atmospheres of Jupiter, Saturn, and Titan, *Int. Rev. Phys. Chem.* **3**, 145–176, 1983.
- Tomasko, M. G., R. A. West, and N. D. Castillo, Photometry and polarimetry of Jupiter at large phase angles: I. Analysis of imaging data of a prominent belt and a zone from *Pioneer 10*, *Icarus* **33**, 558–592, 1978.
- Tomasko, M. G., E. Karkoschka, and S. Martinek, Observations of the limb darkening of Jupiter at ultraviolet wavelengths and constraints on the properties and distribution of stratospheric aerosols, *Icarus* **65**, 218–243, 1986.
- Urban, S., N. Tu, K. Narahari Rao, and G. Guelachvili, Analysis of high-resolution Fourier transform spectra of ¹⁴NH₃ at 2.3 μm, *J. Mol. Spectrosc.* **133**, 312–330, 1989.
- Urey, H. C., ed., *The Planets: Their Origin and Development*, 1952.
- Vasavada, A. R., A. P. Ingersoll, D. Banfield, M. Bell, P. J. Gierasch, M. J. S. Belton, G. S. Orton, K. P. Klaassen, E. Dejong, H. H. Breneman, T. J. Jones, J. M. Kaufman, K. P. Magee, and D. A. Senske, *Galileo* imaging of Jupiter's atmosphere: The Great Red Spot, equatorial region, and white ovals, *Icarus* **135**, 265–275, 1998.
- Vincent, M. B., J. T. Clarke, G. E. Ballester, W. M. Harris, R. A. West, J. T. Trauger, R. W. Evans, K. R. Stapelfeldt, D. Crisp, C. J. Burrows, J. S. Gallagher, R. E. Griffiths, J. Hester, J. G. Hoessel, J. A. Holtzman, J. R. Mould, P. A. Scowen, A. M. Watson, and J. A. Westphal, Jupiter's polar regions in the ultraviolet as imaged by HST/WFPC2: Auroral-aligned features and zonal motions, *Icarus* **143**, 205–222, 2000a.
- Vincent, M. B., J. T. Clarke, G. E. Ballester, W. M. Harris, R. A. West, J. T. Trauger, R. W. Evans, K. R. Stapelfeldt, D. Crisp, C. J. Burrows, J. S. Gallagher, R. E. Griffiths, J. Hester, J. G. Hoessel, J. A. Holtzman, J. R. Mould, P. A. Scowen, A. M. Watson, and J. A. Westphal, Jupiter's latitudinal bands and Great Red Spot using HST/WFPC2 far-ultraviolet imaging, *Icarus* **143**, 189–204, 2000b.
- von Zahn, U., D. M. Hunten, and G. Lehmacher, Helium in Jupiter's atmosphere: Results from the *Galileo* probe helium interferometer experiment, *J. Geophys. Res.* **103**, 22815–22830, 1998.
- Waite, J. H., G. R. Gladstone, W. S. Lewis, R. Goldstein, D. J. McComas, P. Riley, R. J. Walker, P. Robertson, S. Desai, J. T. Clarke, and D. T. Young, An auroral flare at Jupiter, *Nature* **410**, 787–789, 2001.
- Weidenschilling, S. J. and J. S. Lewis, Atmospheric and cloud structures of the jovian planets, *Icarus* **20**, 465–476, 1973.
- West, R. A., *Voyager 2* imaging eclipse observations of the jovian high altitude haze, *Icarus* **75**, 381–398, 1988.
- West, R. A., Optical properties of aggregate particles whose outer diameter is comparable to the wavelength, *Appl. Opt.* **30**, 5316–5324, 1991.
- West, R. A. and P. H. Smith, Evidence for aggregate particles in the atmospheres of Titan and Jupiter, *Icarus* **90**, 330–333, 1991.
- West, R. A. and M. G. Tomasko, Spatially resolved methane band photometry of Jupiter: III. Cloud vertical structures for several axisymmetric bands and the Great Red Spot, *Icarus* **41**, 278–292, 1980.
- West, R. A., D. F. Strobel, and M. G. Tomasko, Clouds, aerosols, and photochemistry in the jovian atmosphere, *Icarus* **65**, 161–217, 1986.
- West, R. A., G. S. Orton, B. T. Draine, and E. A. Hubbell, Infrared absorption features for tetrahedral ammonia ice crystals, *Icarus* **80**, 220–223, 1989.
- Wildt, R., On the chemical nature of the colouration of Jupiter's cloud forms, *MNRAS* **99**, 616, 1939.
- Woeller, F. and C. Ponnampuruma, Organic synthesis in a simulated jovian atmosphere, *Icarus* **10**, 380, 1969.
- Wong, A., A. Y. T. Lee, Y. L. Yung, and J. M. Ajello, Jupiter: Aerosol chemistry in the polar atmosphere, *ApJ* **534**, L215–L217, 2000.
- Wong, A., Y. L. Yung, and A. J. Friedson, Benzene and haze formation in the polar atmosphere of Jupiter, *Geophys. Res. Lett.* **30**, 30–1, 2003.
- Wong, M., G. Bjoraker, M. Smith, D. Flasar, and C. Nixon, Identification of the 10-μm ammonia ice feature on Jupiter, *Planet. Space Sci.* **52**, 385–395, 2004.
- Yair, Y., Z. Levin, and S. Tzivion, Microphysical processes and dynamics of a jovian thundercloud, *Icarus* **114**, 278–299, 1995.
- Young, A. T., No sulfur flows on Io, *Icarus* **58**, 197–226, 1984.
- Young, R. E., The *Galileo* probe mission to Jupiter: Science overview, *J. Geophys. Res.* **103**, 22775–22790, 1998.
- Young, R. E., Erratum: The *Galileo* probe mission to Jupiter: Science overview, *J. Geophys. Res.* **105**, 12093–12094, 2000.
- Zheng, C. and A. Borysow, Modeling of collision-induced infrared absorption spectra of H₂ pairs in the first overtone band at temperatures from 20 to 500 K, *Icarus* **113**, 84–90, 1995.